Nuclear Materials and Energy 20 (2019) 100696

Contents lists available at ScienceDirect

Nuclear Materials and Energy

journal homepage: www.elsevier.com/locate/nme

Physics basis for the first ITER tungsten divertor

R.A. Pitts[a,*], X. Bonnin[a], F. Escourbiac[a], H. Frerichs[b], J.P. Gunn[c], T. Hirai[a], A.S. Kukushkin[d,e], E. Kaveeva[f], M.A. Miller[g], D. Moulton[h], V. Rozhansky[f], I. Senichenkov[f], E. Sytova[a,f,i], O. Schmitz[b], P.C. Stangeby[j], G. De Temmerman[a], I. Veselova[f], S. Wiesen[k]

[a] ITER Organization, Route de Vinon-sur-Verdon, CS 90 046, 13067, St. Paul Lez Durance Cedex, France
[b] Department of Engineering Physics, University of Wisconsin, Madison, WI 53706, USA
[c] CEA, IRFM, F-13108 Saint Paul-lez-Durance, France
[d] National Research Center "Kurchatov Institute", Akademika Kurchatova pl. 1, 123182 Moscow, Russian Federation
[e] National Research Nuclear University MEPhI (Moscow Engineering Physics Institute), Kashirskoe sh. 31, 115409 Moscow, Russian Federation
[f] Peter the Great St.Petersburg Polytechnic University, Polytechnicheskaya 29, 195251 St. Petersburg, Russia
[g] Columbia University School of Engineering and Applied Sciences, New York, New York 10027, USA
[h] CCFE, Culham Science Centre, Abingdon OX14 3DB, UK
[i] Max-Planck-Institut für Plasmaphysik, 85748 Garching, Germany
[j] University of Toronto Institute for Aerospace Studies, 4925 Dufferin St, Toronto M3H 5T6 Canada
[k] Forschungszentrum Jülich GmbH, Institut fuer Energie und Klimaforschung, Jülich, Germany

ARTICLE INFO

Keywords:
ITER
Tungsten
Divertor
Heat fluxes
SOLPS

ABSTRACT

On the eve of component procurement, this paper discusses the present physics basis for the first ITER tungsten (W) divertor, beginning with a reminder of the key elements defining the overall design, and outlining relevant aspects of the Research Plan accompanying the new "staged approach" to ITER nuclear operations which fixes the overall divertor lifetime constraint. The principal focus is on the main design driver, steady state power fluxes in the DT phases, obtained from simulations using the 2-D SOLPS-4.3 and SOLPS-ITER plasma boundary codes, assuming the use of the low Z seeding impurities nitrogen (N) and neon (Ne). A new perspective on the simulation database is adopted, concentrating purely on the divertor physics aspects rather than on the core-edge integration, which has been studied extensively in the course of the divertor design evolution and is published elsewhere. Emphasis is placed on factors which may increase the peak steady state loads: divertor target shaping for component misalignment protection, the influence of fluid drifts, and the consequences of narrow scrape-off layer heat flux channels. All tend to push the divertor into an operating space at higher sub-divertor neutral pressure in order to remain at power flux densities acceptable for the target material. However, a revised criterion for the maximum tolerable loads based on avoidance of W recrystallization, sets an upper limit potentially ~50% higher than the previously accepted value of ~10 MW m^{-2}, a consequence both of the choice of material and the finalized component design. Although the simulation database is currently restricted to the 2-D toroidally symmetric situation, considerable progress is now also being made using the EMC3-Eirene 3-D code suite for the assessment of power loading in the presence of magnetic perturbations for ELM control. Some new results for low input power corresponding to the early H-mode operation phases are reported, showing that even if realistic plasma screening is taken into account, significant asymmetric divertor heat fluxes may arise far from the unperturbed strike point. The issue of tolerable limits for transient heat pulses is an open and key question. A new scaling for ELM power deposition has shown that whilst there may be more latitude for operation at higher current without ELM control, the ultimate limit is likely to be set more by material fatigue under large numbers of sub-threshold melting events.

1. Introduction

Building on about 20 years of physics simulation, engineering design and component testing, the ITER tokamak divertor is the largest and most complex ever to be constructed. When the ITER Organization (IO) was formed in 2007, the divertor was initially designed as a

* Corresponding author.
E-mail address: richard.pitts@iter.org (R.A. Pitts).

https://doi.org/10.1016/j.nme.2019.100696
Received 14 February 2019; Received in revised form 27 June 2019; Accepted 16 July 2019
Available online 18 July 2019

component featuring both carbon fibre composite (CFC) and tungsten (W) armour, with carbon in the high heat flux (HHF) regions to facilitate commissioning and operation in the early, non-active phases of ITER exploitation [1]. Following an initial proposal by the IO in 2011 to abandon the CFC/W design in favour of an all-W variant for the beginning of operations, the decision in 2013 to switch to a fully W armoured component required not only design changes, but new physics analysis of performance at high power in a metal environment with extrinsic radiators for divertor detachment control. An early assessment of the risks engendered by the switch to full-W from the start of operations from the point of view of plasma-wall interactions was published in [2], coincident with the decision to abandon the CFC-W design, followed by the study in [3] of divertor performance and core-edge integration under burning plasma conditions for an impurity seeded (carbon-free) environment. The issue of edge localized mode (ELM) induced W release and transport has also been separately examined in some detail with respect to W core contamination [4,5].

On the eve of component procurement, this paper discusses the present physics basis, developed in support of the final design in the period since 2013, with invaluable and numerous contributions from the research community within the ITER Parties. In common with [2], when the physics basis for the full-W option was first discussed, the starting point is a consideration of required lifetime for the first divertor (Section 2). This can now be updated following the recent completion of a more detailed ITER Research Plan (IRP) [6] accompanying the 2017 publication of the revised ITER Baseline Schedule up to the end of the first phases of fusion power operation.

As the principal design driver, the emphasis in the paper will be on steady state power flux densities in the deuterium–tritium (DT) phases (Section 3), drawing heavily on the "carbon-free" SOLPS-4.3 plasma boundary simulation code database first introduced in [3], itself a more extensive repeat of earlier studies with metal walls but with an older divertor geometry [7]. In addition to discussing some of the key results with regard to divertor performance, the analysis in [3] focused on core-edge integration to examine the impact on the burning plasma operation window of the switch to non-carbon plasma-facing components (PFC) and extrinsic radiators for power flux control. Here, the simulation database is revisited with divertor performance in mind and, in particular the issue of the peak divertor target stationary power flux density, $q_{\perp,pk}$, where the symbol "$\perp$" refers here, and subsequently throughout the paper, to the quantity on the real target surface (hence the quantity most important to those designing the divertor PFCs). An important distinction to make in the context of this power density when discussing modelling results (thus particularly important in this paper), is the power flux density on a toroidally symmetric target, which is the standard quantity produced by 2-D plasma boundary code modelling, and that on a shaped divertor target, which can also readily be extracted from the code calculations. In this paper, the toroidally symmetric value is referred to through the variable $q_{\perp}^{sym}$ with its counterpart with shaping included denoted as $q_{\perp}^{shp}$. Section 3 will discuss the differences in detail.

It has long been asserted in the engineering literature linked to the ITER divertor that $q_{\perp,pk}$ = 10 MWm^{-2} is a value which must be managed by the actively cooled divertor technology and this has been used as the qualification standard for laboratory testing of HHF components. This is indeed the "target" value taken in the very extensive series of SOLPS studies which have been conducted for the ITER divertor over more than two decades, for different design variants, materials (carbon or carbon-free), including evolution of the code itself (particularly the inclusion of neutral–neutral interactions in the kinetic neutral model). But there is a large variation in the predicted value of $q_{\perp,pk}$, which is very sensitive to the operating point, and 10 MW m^{-2} can readily be exceeded. The focus of these code studies has been placed on finding ways of divertor control such that the dual requirements of $q_{\perp,pk}$ at or below the imposed limit and adequate plasma performance to achieve the burning plasma goals, are simultaneously achieved. In the course of developing the coupled core-edge transport model used extensively for analysis of ITER operational scenarios, a set of key discharge control and core-edge interface parameters were identified (Section 3). It was found that restricting $q_{\perp,pk}$ to 10 MW m^{-2} yields a reasonable operational window (the range of viable input parameters which result in acceptable performance of ITER as a fusion device) for most of the assumptions made on the transport properties of the core and boundary plasmas. The value of target loading in ITER is not therefore a prediction of SOLPS modelling, but rather the constraint imposed to restrict the acceptable range of core plasma performance. Although this paper focuses on *divertor* performance and not on the details of the integrated core-edge modelling, it should be clear that all the simulations from the ITER SOLPS database used here have been performed with core compatibility in view.

In reality, it is technology which places the limit on the tolerable $q_{\perp,pk}$. At the time of the very first ITER designs, well before formation of the IO, when CFC was also still envisaged as an option for nuclear operation [8], CFC and W monoblock (MB) technology was under development and neutron irradiated samples were later shown to be able to withstand several thousand stationary cycles at 10 MW m^{-2} and hundreds more at twice this value without failure of the cooling channel (see e.g. [9]). With the decision to begin ITER operations with a full-W divertor, for which the final design is essentially complete, and now with a more precise idea of the Research Plan which defines the conditions and expected lifetime of the first divertor, it is timely to re-examine the criterion on $q_{\perp,pk}$ and ask what should be the real margin on the tolerable value (Section 4).

In the case of transient loads (principally ELMs and disruptions), there has been some advance in physics understanding since the decision to switch to full W (Section 5). A new multi-machine scaling for ELM target energy deposition [10] again provides some margin for ITER in comparison to baseline assumptions at the beginning of the ITER divertor design activities. However, detailed studies in recent years of the consequences of the discrete PFC structure imposed by the need for active cooling, and the experimental observation of material surface degradation under very large numbers of sub-(melting) threshold transients, still impose a very high level of ELM mitigation if risks of lifetime issues are to be minimized. Regarding disruptions, they remain a major threat to component lifetime if not sufficiently mitigated, particularly the consequences of runaway electrons. In the case of disruption-induced thermal plasma loads, specifically at the thermal quench, some benefit is now expected from W vapour shielding.

Overall, a general conclusion of this review of the ITER W divertor physics basis will be that both physics and engineering constraints will likely force stationary high performance operation to be at high divertor neutral pressures, requiring strong volumetric dissipation by seeded, low Z impurity, but hopefully remaining in the partially detached state. It will also find that although there is reasonable confidence from the extensive simulation activity that this expectation can be fulfilled, there remain a large number of questions to be addressed by tokamak plasma boundary and plasma-wall interaction community in the years leading up to ITER operation. The conclusions section of the paper attempts to highlight the key issues.

2. The ITER divertor and expected lifetime

The key physics design features of the ITER divertor are summarized in Fig. 1. Based on decades of divertor research in tokamaks throughout the ITER partners and 20 years of plasma boundary simulation activity, it features deep, baffled vertical inner and outer targets (henceforth referred to as IT and OT respectively), inner and outer reflector plates and a dome structure located under the lower X-point of the magnetic equilibrium, separating the inboard and outboard divertors. A detailed record of the various physics design studies which have been conducted in the years both prior to and after the formation of the IO, may be

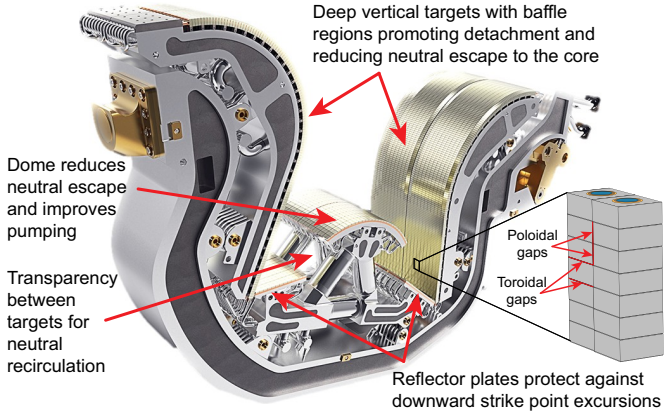

Fig. 1. CAD representation of a single ITER W divertor cassette highlighting some key physics features of the design. Note the strong shaping on the OT baffle for mitigation of downward vertical displacement disruptive loads. The inset shows an example of the vertical target toroidally bevelled monoblocks with the gap naming convention referred to in Section 5.

found in the literature, see [3,7,11–33] for a comprehensive list. In the last of these papers [33], Kukushkin and Pacher provide a brief, yet critical summary of the importance of neutral recirculation within the divertor and how this process is key to controlling divertor operation and performance. In particular, the free neutral particle exchange between the inner and outer divertors is found crucial for reducing in-out target power asymmetries under partially detached conditions. This has been influential in fixing the final ITER divertor design (Fig. 1). The most recent study at the time of writing has focused on the detailed consequences of rigid downward plasma displacements and how the detachment character is modified when strike points access the quasi-horizontal reflector plates [34].

The mechanical/thermohydraulic design has also been the subject of several papers (e.g. [35]). Since the 2013 decision to switch to full-W, the major issue to resolve was the question of surface shaping of the W MBs comprising the inner and outer vertical target armour to protect against eventual misalignments arising during manufacturing and assembly. A great deal of physics activity, both computationally and within the ITER Party experimental facilities (see [36,37]), together with detailed engineering study [38], has now concluded that the W MBs in the HHF regions of the vertical targets will be toroidally bevelled to hide radial misalignments on poloidal gap edges between toroidally adjacent components, but that no shaping solution will be implemented to protect toroidal gap edges between poloidal neighbours. Section 3.2 will return briefly to this decision, the rationale and consequences for stationary power handling.

When discussing the physics basis and in particular the link to *materials*, the required component lifetime is an important factor. The ITER tungsten divertor physics assessment in [2] assumed, as here, that the component is nominally expected to survive until the end of the first DT campaigns. At that time, the precise meaning of “first DT campaigns” was not well defined. Since then, the IO has released a revised Baseline Schedule with a 4-staged approach from first plasma (FP) through to DT operations (Fig. 2), passing through two “Pre-Fusion Power Operations (PFPO) non-active phases (using only hydrogen (H) and helium (He) fuel) before beginning Fusion Power Operation (FPO). From the date of FP (which will be obtained with only temporary in-vessel components), the end of the FPO phase, which defines the lifetime requirement for the first divertor, is expected ~16 years later. The first divertor is to be installed in “Assembly Phase II”, the 2 year period following FP and before the start of the PFPO-1 phase.

Along with the new staged approach, the IO has developed a much more detailed Research Plan [6], from which an approximate idea of the likely number of discharges and plasma exposure time can be derived. Table 1 summarizes the result of this exercise, in which the first part of the FPO phase, up to the achievement of the Project's fusion goals, has been broken down into the three envisaged campaigns (FPO-1-3). At the end of FPO-3, the divertor is expected to be replaced. The numbers in Table 1 have been rounded up and should be taken as indicative only.

It is thus expected that at end of life, the first divertor will have endured $\sim 9 \times 10^6$ s of plasma exposure over a 16 year lifetime, with ~10% of this occurring during the PFPO phases when only H and He fuel will be used and heating powers will, for the most part, be significantly lower than during nuclear operation. The exposure conditions (target particle flux densities, heat fluxes etc., see Section 3) can only be obtained from the kinds of simulation study described here and are in any case uncertain in view of the very large variety of plasma discharges which will be executed in the years leading to the achievement of the principal first goal of burning plasmas at a fusion gain $Q_{DT} \sim 10$. The fact that burning plasmas dominate the integral fluence which will be intercepted by the divertor over its lifetime, justifies the focus of the divertor simulation database on conditions appropriate to FPO. In fact, the FPO-1 phase is largely focused on discharges of shorter flattop duration (e.g. ~50 s), with substantial time dedicated to DD operation, including L-mode development to high current, DD then DT H-mode plasmas at 7.5 MA/2.65 T and finally optimization of DT fusion performance towards $Q_{DT} = 10$ at 15 MA/5.3 T. In FPO-2, approximately half of the programmatic time is foreseen for expansion of operation to full ITER baseline inductive performance ($Q_{DT} = 10$ for durations of 300–500 s). During the latter stages of FPO-2 and throughout FPO-3, emphasis is expected to turn to non-inductive operation at lower plasma current (I_p), lower Q_{DT} and longer pulse length (target is $Q_{DT} \sim 5$ for 3000 s), for which plasma boundary simulations at ITER have not yet begun. Such operation is expected to involve similar powers into the scrape-off layer (SOL), P_{SOL} ~100 MW, as will be the case at $Q_{DT} = 10$, but may have broader heat flux profiles depending on the scaling of the near-SOL parallel heat flux channel width (see Section 3.1.2). The higher q_{95} of these discharges will also modify the wetted area for thermal plasma deposition on the divertor targets (Section 3.2.1). In general, plasma boundary modelling of advanced scenario plasmas on current devices is almost completely absent and the whole issue of the compatibility of a radiative divertor under conditions of non-inductive operation remains largely unexplored.

Neglecting the the PFPO phases, Table 1 shows that the first ITER divertor is expected to be exposed to $\sim 8 \times 10^6$ plasma seconds (~2200 h) during the FPO phases, though not all of this time will be spent under burning plasma conditions and the level of detail achievable at this stage in the IRP does not allow very accurate estimates of the total discharge duration. This estimated exposure time should be compared with the integral campaign exposures on JET with the ITER-Like Wall (ILW), which, at the time of writing, had completed 3 separate campaigns with a total of 27.2 h of plasma in X-point configuration in ILW-1 and 2 [39] and 18.5 h in ILW-3 [40] for a total of 47.5 h of divertor exposure since ILW operation began in 2011. As shown in Section 3 (Fig. 5), integral ion fluences on the ITER divertor targets (sum of IT and OT) at $Q_{DT} \sim 10$ should be in the range (4–8) $\times 10^{24}$ s^{-1} at the higher divertor neutral pressures at which operation is expected (~10 Pa). This can be compared with the integral divertor target fluence measured carefully at JET during a detailed gas balance study performed at the end of the first ILW campaign in which 151 identical Type I ELMing deuterium ELMing H-mode discharges (~9 s H-mode phase in each pulse) were run in a 2 week operational period, yielding 2500 plasma seconds in divertor configuration (with ~1360 s in H-mode) for a total integrated divertor ion fluence of $\sim 5.3 \times 10^{26}$ ions [41]. A similar 2500 s period on ITER during $Q_{DT} = 10$ operation (equivalent to ~5 baseline discharges at maximum expected pulse length) would, according to ITER plasma boundary simulations (Section 3), yield a maximum integrated target fluence of $\sim (1–2) \times 10^{28}$ ions, up to a factor 40 higher than at JET (but more if

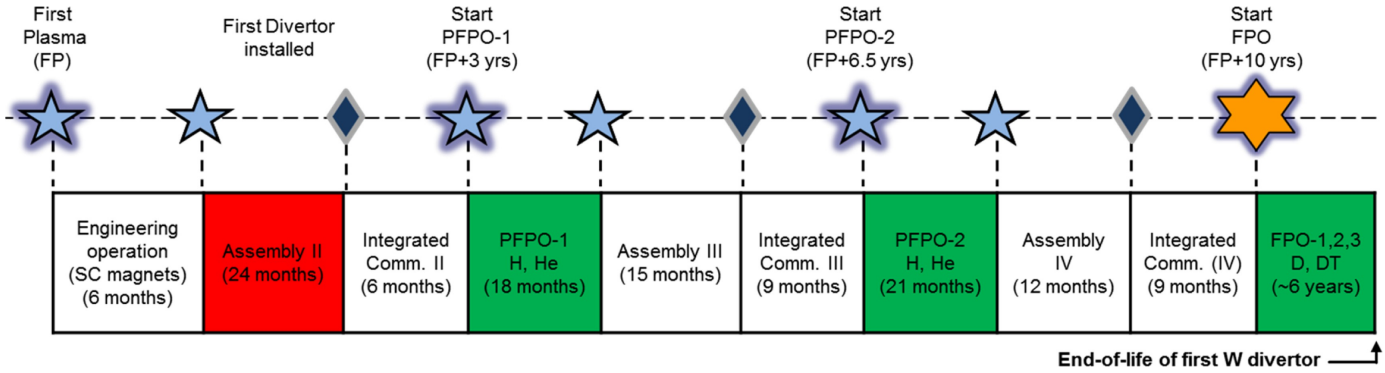

Fig. 2. Schematic breakdown of the revised baseline schedule with 4-staged approach to achievement of burning plasmas. Nominal end of life of the first divertor is the end of the FPO phases.

Table 1
Approximate breakdown of the non-active (PFPO) and active (FPO) ITER campaigns in terms of operation days, pulses and discharge time. Extracted from [6].

Phase	Days	Pulses	Duration (s)
PFPO-1	470	5700	3×10^5
PFPO-2	545	5600	6×10^5
Total PFPO	1015	11300	9×10^5
FPO-1	170	2200	5.5×10^4
FPO-2	415	5400	1.8×10^6
FPO-3	335	4400	6.1×10^6
Total FPO	1090	12000	$\sim 8 \times 10^6$

only the JET H-mode phases are considered). Extrapolating this to the estimated 8×10^6 s of ITER divertor exposure time during FPO (Table 1) gives total integrated fluences of $\sim(1.6–3.2) \times 10^{31}$ ions with peak divertor particle flux densities in the range $\sim 5 \times 10^{23}$ m^{-2} s^{-1} (Fig. 5).

3. Steady state power handling

As the previous section has discussed, the main design drivers for the ITER divertor are the stationary heat fluxes expected during the burning plasma phases. For an actively cooled component, it is the ability to exhaust the incident plasma power with sufficient margin below critical heat flux (CHF) [42] which sets the tolerable peak stationary heat loads (see also Section 4). Sufficient particle exhaust and impurity compression are also critical if core He and impurity content are to remain within acceptable limits for the required fusion gain. Together, these heat and particle exhaust conditions determine the machine steady state operational boundary.

The question of core-SOL compatibility is of critical importance for ITER and reactors in general and has been considered extensively during the ITER divertor design activities (see e.g. [3,21]). The very different characteristic timescales for the core (tens of seconds) and SOL (milliseconds) mean that numerical coupling of the two regions is computationally impractical for the kinds of parametric studies required to scope divertor performance and its effect on the core. The computational challenge is made particularly acute by the extremely long wall clock times required to converge even a single stationary plasma boundary solution if this is performed at the level required for the highest fidelity results (e.g. in terms of overall particle balance). The approach adopted at IO has thus been to produce a series of scaling relationships between key divertor operational parameters (the two most important of which are $q_{\perp,pk}$ and the average divertor neutral pressure, p_n– see Section 3.1.1 for the definition of the latter) and to use these scalings to determine outer boundary conditions for the core (e.g. separatrix D, T, He and impurity densities, ion and electron temperatures and inward neutral DT and He fluxes). The core model (traditionally the 1.5D code ASTRA for the IO studies [[21],[24],[30],[31]) provides input to the scaling relationships (e.g. P_{SOL} and the DT flux into the SOL) and takes as control parameters the core fuelling flux (dominated by pellets in ITER burning plasmas), the puffed gas flux and the additional heating power.

Thus, the overall plasma control parameters (actuators) in the model are the auxiliary heating power, pellet fuelling and gas puffing rates, pumping speed and impurity seeding level. All are real "engineering" quantities, directly controllable, in contrast to a parameter such as separatrix electron density which is often used as a constraint in modelling current devices by virtue of the fact that it is often measured and is thus known. The interface parameters transmitted from the core to the edge models are the flows across the internal grid edge of the power in the fuel ion and electron channels and of the ions of all the species involved (e.g. He and seed impurities). The separatrix-averaged values of the fuel ion and electron temperatures and of the density of all the ion species involved, which form the boundary conditions for the core, together with the neutral flows across the separatrix into the core, which contribute to the core fuelling, are the parameters transmitted from the edge to the core.

More recently, fully coupled core-edge-SOL time-dependent simulations have started to be performed, for example with the JINTRAC code suite (see e.g. [43]), which employs the EDGE2D-Eirene plasma boundary model, a similar code to the SOLPS package which has been the workhorse of the ITER divertor physics design. These fully integrated simulations have the advantage of being able to capture important time dependent features such as ELMs and confinement transitions, but, in the interests of computational time, generally deploy the plasma boundary code in a less intensive manner than for stationary (time independent) simulations (for example launching typically much lower numbers of particles in the Eirene neutral kinetic modelling and ignoring neutral-neutral collisions).

This section now focuses on the database of stationary SOLPS simulations which have been used to scope the ITER divertor operational window and refine details of the design, leaving aside the question of core-SOL integration. Emphasis will be largely on $q_{\perp,pk}$ and its dependence on p_n since both are key controlling parameters. They are strongly linked.

The allowable power flux density is fixed by technology, whereas its actual value is determined mostly by P_{SOL}, the total particle content, N_D and by the impurity concentration in the plasma outside the separatrix, fixed by impurity seeding [44]. Under conditions of strong recycling in the divertor, the particle throughput in the edge plasma is much lower than the recycling fluxes and the timescales for the formation of profiles of plasma parameters in the SOL and divertor are much shorter than those for changing the particle content. It is thus the latter which controls divertor performance.

Whilst N_D is a quantity convenient for simplified theoretical analysis

of divertor performance, it is not practically measurable and therefore of no use for divertor control or interpretation of measurements. In the modelling of current experiments, the upstream separatrix density, $n_{e,sep}$ at the outer midplane (omp) often serves the purpose as a proxy for N_D. It often increases monotonically with N_D and can be measured experimentally. However, for ITER (see Section 3.2.2), $n_{e,sep}$ saturates and even rolls over for high N_D values when detachment deepens. This behaviour can be related to a clear physical picture (see e.g. [44]) in which, depending on the power available for ionization of recycling neutrals, the detached divertor plasma cannot sustain in equilibrium an upstream pressure higher than a given value. In this case, the average neutral density (and hence p_n) in the private flux region (PFR) is a more appropriate metric for N_D. It rises monotonically with N_D until detachment is sufficiently deep that the core plasma collapses and it is related to the particle throughput and pumping speed, both directly controllable engineering quantities.

One key aspect, not treated explicitly in this review, is the issue of detachment control, both in the sense of ensuring that partial detachment is stable and at sufficient degree to maintain heat loads to technologically manageable stationary levels, and that plasma reattachment, if it does occur, is prevented from reaching the point at which the loads approach or exceed values which threaten the integrity of the divertor monoblocks (see Section 4). The precise control methodologies which will be used on ITER are still under development and will all be exhaustively tested in the non-nuclear phases of the IRP. Several options are possible given the very extensive set of diagnostics (e.g. divertor neutral pressure gauges, Langmuir probe and thermocouple arrays, total radiation bolometry, infra-red thermography, divertor spectroscopy etc.) with which ITER will be equipped (see e.g. [45]). Some of these options have already been tested to a greater or lesser extent on current devices and it is important that this effort intensifies as ITER construction proceeds.

3.1. The ITER SOLPS simulation database

Presented for the first time in [3], the existing ITER divertor plasma boundary simulation database for the metallic PFC environment in baseline burning plasma conditions (Q_{DT} = 10) and the final divertor geometry consists of ~125 validated cases with Ne seeding and a much lower number for N-injection, for which more expanded studies are now ongoing. This database of SOLPS-4.3 code (comprising the two-dimensional B2 fluid plasma and the three-dimensional Eirene Monte Carlo kinetic neutral codes) runs is now being fully transferred into the ITER Integrated Modelling Analysis Suite (IMAS) [46] and each run is associated with a unique case number, as is the case henceforth for all new simulations. The latter are now mostly being produced with the SOLPS-ITER code (B2.5 fluid plasma and Eirene Monte Carlo kinetic neutral codes), the most up-to-date version of the SOLPS suite, launched by the IO in 2015 [47,48]. Beginning with a description of the most important code inputs for the main (SOLPS-4.3) database (Section 3.1.1), the following sub-sections describe a selection of key findings which can be derived from the simulations.

3.1.1. Code inputs and definitions

To-date, the "carbon-free" SOLPS simulation database uses exclusively the baseline ITER inductive magnetic equilibrium at q_{95} = 3, and assumes Type I ELMing H-mode operation, the regime of the discharges constituting the multi-machine database used to derive the IPB98(y,2) scaling for the ITER thermal energy confinement time [49]. For Q_{DT} = 10 burning plasmas (the main concern here), q_{95} = 3 is obtained at plasma current and toroidal magnetic field of I_p = 15 MA, B_φ = 5.3 T respectively, but equally at one half and one third values (5 MA/1.8 T and 7.5 MA/2.65 T), both of which figure prominently in the new IRP [6] to progressively approach full performance. The equilibrium features high upper triangularity (δ ~ 0.5) and outer midplane separation between the first and second separatrices of

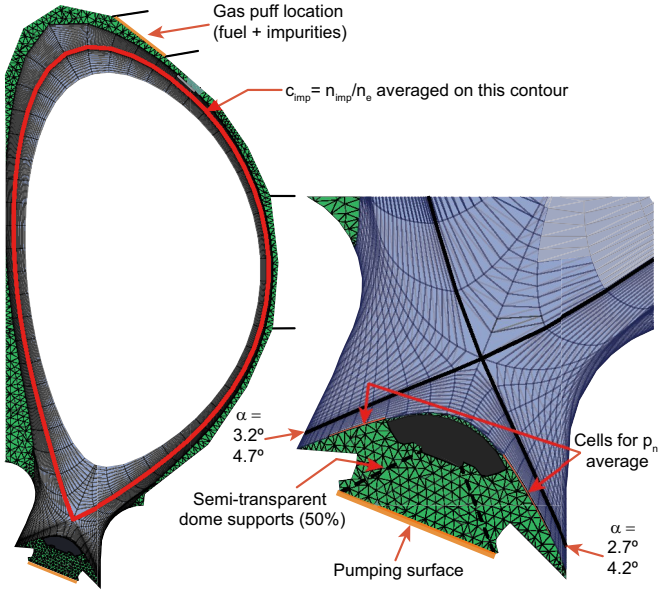

Fig. 3. The SOLPS-4.3 and SOLPS-ITER numerical grid generated from the nominal ITER baseline magnetic equilibrium at q_{95} = 3. The expanded region provides more detail in the divertor. The neutral and plasma fluid grids overlap in the plasma grid region. Impurity concentration is averaged along the marked poloidal ring.

Δr_{sep} ~ 9 cm. The latter is adopted to allow for more margin with respect to upper main chamber PFC loading, but can of course be varied (the ITER Project Requirements allow values as low as Δr_{sep} ~ 4 cm [50]).

Fig. 3 illustrates the SOLPS computational mesh used in the ITER studies, derived from the baseline equilibrium, including an enlarged view of the divertor region and showing how the fluid plasma (quadrangular) grid is limited by the second separatrix, with the Eirene code (triangular) grid extending out to the domain walls. The separate two grids completely overlap in the plasma region.

An important parameter determining the target power flux densities is the total incidence angle, α between the target surface and the magnetic field lines. Its value at the IT and OT strike points is marked in Fig. 3, both for the pure cylindrically symmetric case assumed in SOLPS (which is a 2D model) and the (higher) value obtained when component surface shaping is taken into account For the ITER divertor, the final shaping decision (see Section 3.2.1 and [36]) increases the strike point angle by 1.5° compared to a perfect, toroidally symmetric target.

There are several key input specifications and general characteristics of the main database simulations which are of importance for this paper (see also Fig. 3):

1) Since the B2 code contains no drift terms in the fluid equations, SOLPS-4.3 simulations do not include drifts and currents.
2) Simulations are steady state: ELMs are included only implicitly in that it is assumed that they will carry some fraction of P_{SOL} (typically in the range 20–40% for Type I ELMs [2]). This is a reasonable approach from the point of view of global power balance, but does not of course take into account any possible modifications of the target power load profiles during the ELM. The latter aspect has in fact been investigated at the IO in an unpublished study in which a series of SOLPS-4.3 stationary IT and OT profiles for varying p_n have been combined with simulations of ITER Type I ELM target heat flux profiles [51] obtained with the 3D non-linear MHD code JOREK (for the specific case of a relatively low ELM plasma energy loss of 4 MJ). Normalizing the peak power flux density to a fixed value determined by an average stationary load consistent with the combined inter-ELM and ELM power fluxes (the sum of which must

equal P_{SOL}), the study found that including the ELMs led to only very minor variations in the SOLPS stationary power flux density profile. Similar conclusions may not be possible for much larger ELMs, which will be found on ITER if no mitigation measures are taken. These transients, occurring at much lower frequencies, are likely to significantly broaden the power deposition on the targets, but are quite simply (Section 5) unacceptable from the target lifetime point of view. The very small ELMs which may be tolerable for the target (Section 5) are not expected to broaden the deposition profile compared to the inter-ELM situation.

3) Even though the $Q_{DT} = 10$ burning plasma is an H-mode, an "L-mode" edge (i.e. no H-mode pedestal) is assumed in the SOLPS-4.3 simulations. This is not the case for the newest SOLPS-ITER code runs reported here (see Section 3.2.2), which include drifts and a full H-mode pedestal.
4) Like the majority of current plasma boundary simulation packages, SOLPS is not a turbulence code and requires user specified anomalous cross-field transport coefficients for particles ($D_\perp$) and heat ($\chi_\perp$). Almost all current entries in the simulation database use $D_\perp = 0.3\ m^2\ s^{-1}$ and $\chi_\perp = 1.0\ m^2\ s^{-1}$ (fixed at all radial and poloidal cells in the numerical grid) for both main ions, impurities and electrons, with the power injected across the inner core boundary of the numerical grid, split equally between ions and electrons. As discussed in more detail below, this leads to a fixed value of the radial decrease of heat flow parallel to the magnetic field in the near SOL (λ_q). No radial pinch velocity is specified. At the outer edge of the plasma grid, radial decay lengths of 3 cm for all densities and temperatures are set as boundary conditions at all poloidal locations. Note that the power entering the inner core boundary is denoted here by P_{SOL}, even though this is not strictly the power crossing the separatrix in the simulations. The difference is minor since radiative power losses in the thin inner core region of the simulations are at most a few percent even at the highest impurity concentrations.
5) The simulations are multi-fluid, accounting for seeded impurity (Ne or N), D (representing both D and T isotopes) and He (produced by fusion reactions). Fixed ion fluxes into the simulation domain are imposed across the inner core boundary of the plasma grid of D^+ ($9.1 \times 10^{21}\ s^{-1}$) and He^{2+} ($2 \times 10^{20}\ s^{-1}$), consistent with core fuelling and fusion power production at $Q_{DT} = 10$ and $P_{SOL} = 100$ MW. Note that the results are not very sensitive to the level of D^+ core fuelling [32]. It is the total particle throughput which determines p_n and controls divertor performance.
6) For simplicity (to avoid a great many additional ion fluids, even with W bundling), the SOLPS-4.3 simulations do not include any W surfaces in the divertor. For the vast majority of the conditions examined, the divertor target plasma is too cold for much W erosion to occur, except during ELMs, which are not explicitly simulated (though see Section 5 concerning the impact of ELM-induced sputtering on the allowed ELM frequencies). Instead, Be eroded from the main chamber walls is assumed to migrate everywhere into the divertor, coating the targets but with no Be re-erosion, so that the code assumes energy and particle reflection coefficients for a Be substrate (see Section 3.1.5 for further brief discussion on this matter). A few scoping runs with Be erosion activated found only a minor supplement to the total radiation (and hence dissipation in the divertor), which is dominated by the contribution from fuel atoms and extrinsic seed impurity. The assumption of a fully Be coated IT is consistent with WALLDYN simulations for ITER burning plasmas conducted in [52], but is not supported by these same calculations at the OT, where, depending on the operating point, the surface temperature would be too high for Be to remain. This may not be the case if the divertor is operated at high neutral pressures, when the surface temperature at both IT and OT will be low (see Section 4 and Fig. 17).
7) The impurity and fuel ions are injected in the simulations across a poloidally extended low field side region of the main chamber corresponding to the location of the upper lateral ports. This choice is somewhat historical since the real gas puff locations were not fully decided at the time the simulation database was being constituted. Out of the 10 gas lines which will be installed in ITER [53], 4 will enter through the upper ports. However, the injection point will now be displaced toroidally and poloidally (towards the omp) from the port, with the end of the injection nozzle located in a gap between adjacent blanket modules (BM). Gas dynamic simulations demonstrate that although there will evidently be a peak of injected flux at the nozzle location, the gas will also diffuse within the blanket module structure and will enter the chamber over a much wider region through the gaps between BMs. This shift in the poloidal injection location compared to that specified in the simulations will not impact the results, particularly in view of the high opacity of the ITER burning plasma SOL [22]. The remaining 6 lines will enter through the lower ports at divertor level and will feed toroidal loops attached to the vacuum vessel floor below the divertor cassettes, allowing for quasi-toroidally uniform injection. It is currently expected that these lines will in fact be the primary vehicle for divertor detachment control through impurity and fuel gas injection. New simulations [54] are now ongoing with SOLPS-ITER to examine the influence of divertor versus main chamber injection. First results confirm the expectation of a rather weak influence in these steady state simulations: once ionized, the injected gas components will rapidly distribute in the boundary plasma on SOL transport timescales (ms), though main chamber injection (and this is seen in both the SOLPS-4.3 and SOLPS-ITER simulations) does have a strong local effect on the SOL density at the injection point.
8) Along with the fuel throughput, the impurity concentration, $c_{imp} = n_{imp}/n_e$ is the principle variable in the $P_{SOL} = 100$ MW database. Here, the average of c_{imp} in all cells of the first poloidal ring outside the main chamber separatrix, from X-point to X-point is used as the metric to classify the simulation cases. Although the impurity level could be characterized by different quantities, this separatrix-averaged, relative ion impurity concentration is most convenient for coupling to a core model and this has been the key-point in all SOLPS-4.3 modelling for ITER since 2003 [3,7,14–32]. The first SOL ring outside the separatrix is used in the definition to avoid uncertainties due to the lack of a proper core model in the simulations. In practice, to generate the scans of c_{imp} for various p_n in the database, the ratio of fuel to impurity puffing is controlled through the use of feedback loops in the simulations.
9) The key parameter p_n is defined as the average of the neutral pressures (computed in Eirene) over the parts of the PFR boundary which face the dome support openings (see Fig. 3 and [20]). This choice is historical and was made in an early stage of development of the Eirene code when neutral-neutral collisions were not modelled and neutral gas parameters were calculated only on the B2 plasma grid. The definition was maintained for backwards compatibility: although the absolute value of p_n is not so important, the definition must be maintained for meaningful comparisons. Note that the Eirene simulations present in the ITER database employ the "Kotov model" [55] for collisions between fuel atoms and molecules (in this case D/D_2 neutrals and charged species). The impact of molecular vibrationally excited states is included in the quasi-static approximation in which the timescale for equilibration of the vibrational state population is faster than transport times. Neutral–neutral elastic collisions for all pairs of species in the simulations are also included (e.g. D–D, D–D_2, D_2–D_2, D–Ne, D_2–Ne, Ne–Ne, D–N, D_2–N, N–N), using a constant cross-section corresponding roughly to a hard-sphere approximation. It should be noted that a very extensive set of in-vessel fast pressure gauges are foreseen in several cassettes of the ITER divertor [45]. As such, the key parameter p_n, listed in the ITER Project Requirements as a main

parameter for machine control, should always be measurable.

10) In the simulations, 100% recycling of D and He at all material surfaces is imposed (thus unity recycling coefficients for ions and unity total neutral reflection coefficients) and pumping is modelled by specifying an absorption coefficient for neutrals at the pump duct, defined as the lower boundary of the Eirene grid below the divertor dome (see Fig. 3). This value is fixed at 0.72% for all simulations and has been adjusted to match a physical "engineering pumping speed" ($\sim$60 m^3 s^{-1}) at the pumping duct which determines the throughput (pumped flux) for given p_n [20].

3.1.2. Near SOL parallel heat flux width

Returning to point 4 in the list above, the issue of the appropriate value of λ_q for ITER under baseline burning plasma conditions is currently the subject of considerable debate. Empirical scaling from multi-machine infra-red thermography measurements of outer target inter-ELM power loads under attached divertor H-mode conditions found a clear $\lambda_q \propto 1/B_\theta \propto 1/I_p$ dependence (B_θ is the poloidal field at the omp), extrapolating to $\lambda_q \sim 1$ mm on ITER at 15 MA [56]. An analytic "heuristic drift" theory in which neoclassical ion drifts are balanced by sonic parallel flows in the SOL out to the divertor also found a strong inverse dependence of λ_q on I_p and quantitatively matched the experimental scaling results [57]. More recent analytic work on the structure of the near SOL [58] with little or no anomalous radial transport, supports the conclusions in [57] and further demonstrates that the SOLPS-ITER code with drifts activated reproduces the finding when cross-field transport is strongly reduced. Additional experimental measurements performed since the multi-machine work in [56] was published show that the empirical scaling is followed also on COMPASS [59] and Globus-M [60], much smaller devices than those comprising the initial study, and on the C-Mod tokamak, operating at much higher B_θ than any point in the existing database [61]. This latter study is particularly significant given that it extends the scaling to values of B_θ even beyond the ITER value at 15 MA.

In contrast to these extremely narrow predicted heat flux widths, a key result from state-of-the-art simulations of attached divertor conditions on ITER with the 3D particle-in-cell based edge (electrostatic) gyrokinetic code XGC1 is that at high current on ITER, the contribution of cross-field electron turbulence (radial streamers) dominates over the neoclassical magnetic ion drifts, yielding $\lambda_q \sim 6$ mm [62]. The same code and methodology applied to current devices, reproduces closely the experimentally observed $\lambda_q \propto 1/B_\theta$ scaling. In the latest development of the work in [61], an XGC1 simulation of a lower power ITER plasma at $I_p = 5$ MA yielded a λ_q close to the experimental regression value [63]. The proposed explanation for the transition from the magnetic drift to the turbulence dominated regimes is an electron turbulence bifurcation from "filament-like" to "streamer-like". Simulations are in progress to establish at what values of parameters in ITER the transition occurs.

In a parallel approach, the 3D BOUT++ 6-field, 2-fluid electromagnetic model is being used to model the near-SOL λ_q, both on current devices and on ITER [64]. Similar to the XGC1 simulations, BOUT++ begins with a set of pedestal profiles and a magnetic equilibrium for any given device; for ITER these are supplied through separate transport simulations, but are prescribed experimentally for present devices. The code finds $\lambda_q \sim 5$ mm for $I_p = 15$ MA operation at $Q_{DT} = 10$. This is remarkably similar to the XGC1 result, but occurs for different reasons (due to peeling-ballooning turbulence). In common with XGC1, BOUT++ simulations also find good agreement with present machines, with the predicted λ_q following the experimental $1/B_\theta$ scaling, even for the newest results from C-Mod [61] at ITER-relevant B_θ.

To overcome the problem of timescales (the large disparity between electron and ion SOL transit times ($\sim$100 μs vs. $\sim$10 ms) precludes reaching saturation of the divertor ion heat flux during the turbulence simulation), a separate "transport" model has been developed inside the BOUT++ framework. The model includes electric and magnetic drifts, with the same flux-limited parallel thermal SOL transport as in the full turbulence model, but with SOL cross-field transport specified rather than evolving self-consistently from the turbulence (transport coefficients in the pedestal are computed from experimentally measured or prescribed pedestal profiles of n_e, T_e, T_i). The total (ion + electron) divertor heat loads are obtained assuming toroidal symmetry, using the 2-D option in the code. Sensitivity studies are performed with the SOL $\chi_\perp$ varying over a wide range (for fixed $D_\perp$).

The principal finding of this study is that there exists a critical value $\chi_{\perp c}$ below which the divertor heat flux width is insensitive to the SOL thermal diffusivity so that drifts dominate cross-field transport and the simulated heat flux widths are in good agreement with the experimental scaling and Goldston's Heuristic Drift model [57]. For $\chi_\perp > \chi_{\perp c}$, turbulence dominates and the heat flux width increases with increasing $\chi_\perp$. Simulations performed for C-Mod and ITER indicate that $\chi_{\perp c}$ depends on machine size (and/or on pedestal structure), so that $\chi_{\perp c}$ is much smaller for ITER than C-Mod at similar B_θ. As a consequence, turbulence dominates over magnetic drifts and the empirical scaling [56] is broken for ITER.

It is thus not yet possible to state with confidence what the burning plasma, 15 MA heat flux width should be on ITER, but a choice of anomalous cross-field transport coefficients must be made for the divertor plasma simulations. The values fixed for the simulation database ($D_\perp = 0.3$ m^2 s^{-1} and $\chi_\perp = 1.0$ m^2 s^{-1}, see point 4) above) are in fact retained from earlier studies with carbon targets, where the choice was made based on simple ballooning stability arguments [65] which indicated $\lambda_q \sim$ few mm, long before the recent experimental scalings and theoretical work were available. Fig. 4 uses the approach first introduced in [28] to characterize the upstream near SOL parallel heat transport in the ITER SOLPS-4.3 Ne-seeding simulation database. The symbols represent the poloidally averaged Ne concentrations as defined in Point 7) above (see also Fig. 5) and points from all 53 simulation cases selected from the database (used throughout the rest of this section) are plotted. These cases cover a wide range of fuel and impurity throughput, giving $n_{e,sep} = 3$–6×10^{19} m^{-3} (see also Fig. 15a). All have $P_{SOL} = 100$ MW.

Illustrated by the inset in Fig. 4, the procedure is to extract the radial profile of parallel heat flux density, $q_{||}$ just above the entrance to

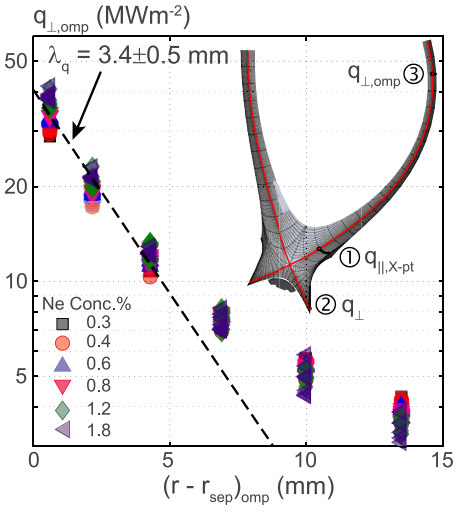

Fig. 4. Outer target perpendicular heat flux density profiles mapped to the omp for the 53 cases in the SOLPS-4.3 simulation database sorted by Ne concentration ($P_{SOL} = 100$ MW). The mapping procedure is described in the insert. Note that the "divertor entrance" profile (Step 1) is taken slightly above the X-point to avoid "blurring" of the profile due to reverse flows which are often seen in the simulations at the separatrix in the X-point vicinity [29]. The dashed line is the average of all the individual fits for each profile.

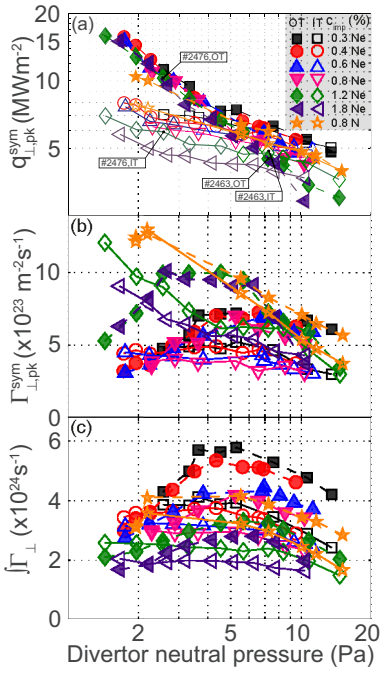

Fig. 5. Divertor neutral pressure variation of peak target heat flux density, peak ion flux density and integral plate ion flux (IT + OT) for the Ne-seeded cases of Fig. 4 (P_{SOL} = 100 MW). A single N-seeded series is also included. The 4 identified simulation case numbers are used later in Fig. 12 to illustrate the p_n variation of the separate contributors to $q_{\perp,pk}$. Open symbols, IT, closed OT. Symbols and colours will be preserved in most subsequent figures. Note that peak heat and ion fluxes are the toroidally symmetric values with no account taken of target shaping.

the outer divertor (Step 1) and then (Step 2) map this to the OT, projecting onto the target, taking into account the full variation of angle of incidence of the field lines and variations in total flux expansion and therefore excluding any of the divertor dissipation effects on $q_{||}$ which the code accounts for. Finally, this profile of $q_{\perp}$ is mapped back up along flux surfaces to obtain the radial profile of heat flux density on the target *at the omp* (Step 3). Each SOLPS simulation thus produces one profile of $q_{\perp,omp}$ and the values on the first 3 numerical grid cells (corresponding to the near SOL) are fitted with a simple exponential ($q_{\perp,omp} = q_0 \exp(-(r - r_{sep}/\lambda_q)$, with q_0 the heat flux density at the separatrix. The average of all these fitted values gives $\lambda_q \sim 3.4 \pm 0.5$ mm.

What is important to note from Fig. 4 is that despite the very wide variation in divertor parameters found in the database (as shown in the following sub-sections), the upstream λ_q is essentially unchanged. Similarly, at fixed impurity concentration, $n_{e,sep}$ is relatively insensitive to fuel throughput (see Section 3.2.2). This can be taken as evidence that within the range of fuel and impurity throughputs included in the database, the divertor is efficient at screening the main SOL. A value of $\lambda_q \sim 3.4$ mm is clearly significantly higher than the ~1 mm widths predicted by the empirical scaling (and the neoclassical ion drift model) discussed above, but is less than a factor ~2 lower than found in the XGC1 or BOUT++ simulations. Since $q_{||} = \text{const}/\lambda_q$ for fixed q_{95}, R and P_{SOL}, it is clear that a factor 3 lower λ_q will yield $q_{||}$ at the divertor entrance higher by the same factor, requiring stronger dissipation to achieve detachment. The consequences for divertor power loading under dissipative conditions of a much lower λ_q than the characteristic value for the simulation database will be discussed further in Section 3.2.2.

3.1.3. Operating window in peak power flux density

Fig. 5 summarizes the divertor target response at both targets, in terms of peak perpendicular power load, $q^{sym}_{\perp,pk}$ (Fig. 5a), peak ion flux density, $\Gamma^{sym}_{\perp,pk}$ (Fig. 5b) and integral ion flux to the plate (Fig. 5c) for a selection (comprising 53 cases) of the Ne-seeded simulation database sorted by c_{Ne} and plotted against the averaged divertor neutral pressure defined in Section 3.1.1. Here, as defined in Section 1, the superscript "sym" now denotes the standard cylindrically symmetric quantity provided by SOLPS, thus assuming a perfect toroidal target with no shaping. A few selected points for N seeding at $c_N = 0.8\%$ (P_{SOL} = 100 MW) have been added for comparison (the database is currently much more restricted for nitrogen impurity). The peak power density includes all contributions to the target heat load: thermal plasma, energy due to recombination at the plate, charge exchange (CX) and photon loads, but does not account for divertor target shaping, of which the CX neutral and photon loads are independent. The effect of shaping will be discussed in Section 3.2.1 (Fig. 12), which will use the 2 specific simulation cases identified in Fig. 5a to take a closer look at the various loading contributions.

The $q^{sym}_{\perp,pk}$ vs. p_n plot in Fig. 5a is the key operating curve for the ITER divertor. It shows that for high neutral pressures ($p_n \sim 10$ Pa), the outin target peak heat flux densities essentially symmetrize for all impurity seeding rates, whilst maintaining partial detachment (Fig. 5b and c, where the peak and integral plate ion fluxes remain significant even at high p_n). This reduction in the target power density asymmetry is not driven in these simulations by a drift effect, since SOLPS-4.3 does not include drifts and currents. One contributor is the strong neutral convection from inner to outer target through the PFR balancing ion flow from outer to inner target through the SOL [66]. The transparency for neutral recirculation afforded under the dome by the relatively widely spaced dome struts is critical in this respect (Fig. 1) and is one of the examples of how these divertor simulations have influenced the overall design of the component. It can be seen, in fact, that in some cases, particularly at high c_{Ne}, the power density maximum occurs at the IT for high p_n. Another important feature of this simulation study, addressed later in Section 3.2.2 (see Fig. 15a) is that an increase in c_{imp} leads to a reduction in $n_{e,sep}$ for the same divertor performance (i.e. same p_n and $q^{sym}_{\perp,pk}$). This opens up another direction for optimization of the core plasma [3].

Although not shown here, operation at high throughput (high p_n) is also favourable for He exhaust, which improves rapidly as the neutral pressure rises and detachment deepens. This was seen clearly in the early ITER divertor simulations studies with carbon targets (see e.g. Fig. 2b in [12]). The same behaviour is recovered in the "carbon-free" database discussed here, for which the scalings for core-edge integration developed in [3] show a reduction in upstream separatrix He ion density and He neutral influx to the core with increase of p_n. The issue of at what point (i.e. which level of detachment) this trend fails, has not yet been systematically studied. Fundamentally, He exhaust improves at higher p_n, because the plasma temperature in the divertor is lower and the ionisation mean-free path for the He atoms recycling off the target increases, so more He reaches the PFR where the pumping duct is located.

At the lowest values of p_n in the scan ($\lesssim$ 3 Pa), where thermal plasma loading dominates the total heat load (Section 3.2.1), $q^{sym}_{\perp,pk}$ at the OT readily exceeds the ~10 MW m^{-2} level often cited as the ITER divertor stationary power handling limit (Section 4 discusses the real limit). At the IT, power densities are much lower, reflecting the natural asymmetry which is expected to arise (in the absence of drifts) in these kinds of simulations: for poloidally uniform radial transport, toroidal geometry and the Shafranov shift push more power to the outboard target [67], though the steeper poloidal inclination of the IT partially compensates (approximately by the ratio of the total impact angles at the strike points: 3.2/2.7 ~ 1.2 – see Fig. 4) when considering peak power flux density.

For forward toroidal field direction as in ITER ($\mathbf{B} \times \nabla B$ drift direction towards the lower X-point), drifts would be expected to further

enhance the out-in power asymmetry, though for ITER, first SOLPS-ITER simulations with drifts activated are indicating that at least for higher p_n, their effects are low (Section 3.2.2). As pointed out already in [3], at the OT $q_{\perp,pk}^{sym}$ is insensitive to c_{Ne} at low p_n, but branches into two zones with increasing p_n, dependent on the magnitude of c_{Ne}. This flattening out of the $q_{\perp,pk}^{sym}$ at higher pressures is due to an increasing contribution of perpendicular loads to the target as detachment deepens: the plasma thermal and plate ion recombination contribution to the total load decreases, and is replaced by photonic radiated and CX neutral loads, which together give a roughly constant power flux density with increasing p_n (see also Section 3.2.1). It is clear that very little impurity seeding is required at high p_n and $P_{SOL} = 100$ MW to keep $q_{\perp,pk}^{sym}$ to acceptable levels. This can also be interpreted as a useful advantage in terms of operations since when operating at higher neutral pressure (favourable also for He exhaust), there will be some margin in the required accuracy for impurity gas dosing.

Fig. 5c illustrates one of the features of the simulation database in the context of detachment. In all studies of the ITER divertor performance thus far, an "edge-based density limit" (at which point neutral escape to the main chamber would be excessive) has been fixed at the point corresponding to full detachment of the inner target, which usually detaches earlier than the outer for given fuel/impurity throughput. Simulations have not yet been strongly pursued beyond this point. For the purposes of core-SOL integration [3], (partial) detachment is defined, rather arbitrarily, as the value of p_n at which the integral OT ion flux falls to 80% of its maximum value, corresponding to $p_n \sim 10$ Pa in Fig. 5c. At the IT, the detachment degree is higher for given $p_n$and the turnover in total ion flux is less marked.

To see the nature of the detachment in more detail, Fig. 6 compiles a set of OT target profiles ($q_{\perp}^{sym}$, $\Gamma_{\perp}^{sym}$, electron temperature and density, $T_{e,t}$, $n_{e,t}$) from the series at $c_{Ne} = 1.2\%$ in Fig. 5. The profiles of $q_{\perp}^{sym}$ (Fig. 6a) follow nicely the schematic description of partial detachment in a vertical target configuration introduced in [68]. Beginning from an attached state at lowest p_n, the peak power flux density reduces steadily with increasing throughput and moves outward away from the nominal strike point position. Perpendicular diffusion into the PFR shifts the peak slightly away from the strike point at low recycling. These low neutral pressure cases have high $T_{e,t}$ (Fig. 6b) and may not, in fact, be sustainable from the point of view of W release, though, as discussed in Section 3.1.1, the SOLPS-4.3 simulations do not include W sputtering, or even W surfaces.

For $p_n \gtrsim 3$ Pa in this particular run series, $T_{e,t}$ in the strike point vicinity begins to fall to very low values (< 1 eV, see also Fig. 10 and Section 3.1.5), but the ion flux (Fig. 5d) continues to rise, broadens and eventually saturates before starting to fall for $p_n \gtrsim 7$ Pa, at which point $T_{e,t}$ collapses across the entire target. The ion flux nevertheless remains high in the outer part of the divertor SOL, maintaining sufficient neutral plugging and preventing the escape of too many neutrals to the main chamber. This is one of the main advantages of the vertical target configuration and is also the reason why full ion flux detachment across the target is to be avoided. To demonstrate this further, Fig. 7 takes the same series of cases at $c_{Ne} = 1.2\%$ in Fig. 6 and examines the variation of the total pressure (static + dynamic) profiles upstream, $p_{tot,u}$ (at the omp) and outer target, $p_{tot,t}$ across the throughput (p_n) scan. Here the pressure is computed as $p_{tot} = k(n_e T_e + n_i T_i)(1 + M^2)$ [69] with M the plasma flow Mach number ($M \equiv v_{||}/c_s$ with c_s the sound speed and $v_{||}$ the parallel flow velocity). Fig. 7 illustrates well how the ratio $p_{tot,t}/p_{tot,u}$ decreases and the region of downstream pressure loss increases with increasing p_n. For all values of p_n, the upstream pressure profile is essentially unchanged, illustrating again (see discussion in Section 3.1.1 on the constancy of λ_q) the insensitivity of the main chamber SOL to strong variations in the divertor. Beyond the region of pressure loss, where the detachment occurs, the upstream and target profiles overlap nicely.

The apparent overpressure for the more attached cases at lower p_n (high $T_{e,t}$ and low collisionality) was attributed in [69] to parallel

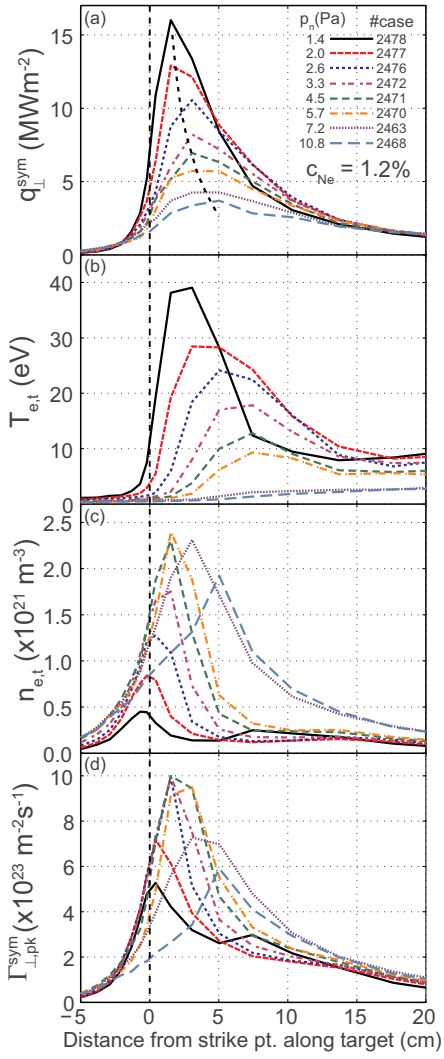

Fig. 6. Outer target profiles of perpendicular heat flux, electron temperature, electron density and perpendicular ion flux density with increasing p_n for the scan at fixed $c_{Ne} = 1.2\%$ and $P_{SOL} = 100$ MW in Fig. 5, illustrating the progression through attached, to high recycling and partially detached states.

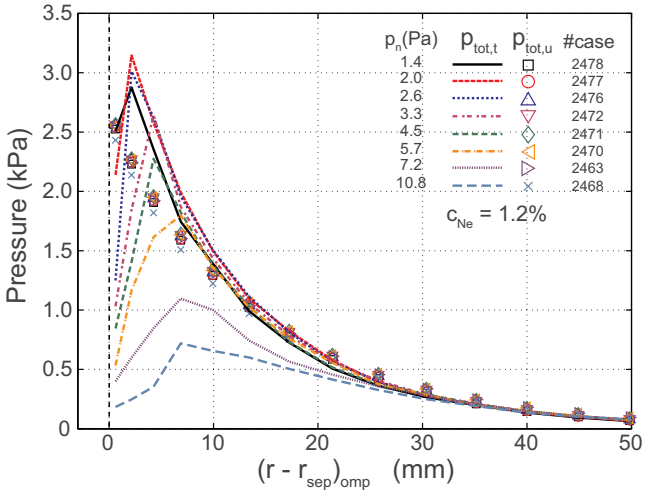

Fig. 7. Variation of upstream and outer target total pressure profiles (mapped to the omp) at $c_{Ne} = 1.2\%$, $P_{SOL} = 100$ MW for the same scan in p_n as in Fig. 6.

viscosity and in [29,70] to a combination of parallel viscosity and reverse ion flow which ensures particle balance along the most loaded flux tubes where the ionization source is much stronger than the ion flux from further upstream. The magnitude of the parallel viscosity is dependent on the applied ion viscosity limiter in the code. The issue of what exactly drives the ion flux reduction nearer the separatrix will be revisited briefly in Section 3.1.5, along with further discussion on pressure-momentum losses.

3.1.4. Divertor radiation

Effective confinement of low Z impurities seeded extrinsically for detachment control is a key function of the ITER divertor. An important issue for future ITER operation is the question of which divertor seed impurity (N or Ne) is most appropriate. Unsurprisingly, given the proximity of the radiation functions between C and N, nitrogen seeding provides the best performance experimentally in current devices with respect to older results in an all-C environment. However, the formation of ammonia during N injection in all-metal tokamaks [71] is expected to be an issue for ITER, mostly in the sense of a limitation on the achievable duty cycle.

Tritiated ammonia is efficiently retained on the active charcoal used in the ITER divertor cryopumps and can only be recovered by full regeneration. For safety reasons, the cryopump tritium inventory cannot exceed 180 g and regular regenerations (to ~100 K) will be performed during operations to recover the pumped hydrogenic species, a process which requires ~600 s, but which would not allow for ammonia recovery. Regenerations at higher temperature, whilst of course possible, are very time-consuming (about 6 h per pump, 6 pumps) so that significant ammonia production could strongly affect the ITER duty cycle. The formation of tritiated ammonia also has an impact on the design of the tritium plant, which needs to be able to decompose ammonia to recover tritium and at the same time avoid the formation of deleterious nitrogen oxides.

Although it is clear that ammonia formation proceeds through surface reactions between nitrogen and hydrogenic radicals, the relative extent to which these reactions proceed on plasma-exposed or plasma-shadowed areas remains to be quantified and it is, therefore, currently not possible to predict the ammonia formation rates to be expected in ITER. Steps are being taken to improve this situation with the recent development (under contract to the IO) of the AMMONX database describing nitrogen chemistry for inclusion into Eirene [72]. The possible impact on the IRP of using N-seeding has thus not yet been assessed, but Ne is likely to be the preferred alternative if it is found to perform similarly with regard to plasma performance, with the added benefit that its property as a fully recycling gas may extend the timescales for avoidance of divertor MB overheating in the event of loss of seeding or other divertor reattachment events.

The very extensive experiments performed in recent years in the full-tungsten ASDEX Upgrade with ITER-relevant divertor geometry (see e.g. [73]) have clearly demonstrated that N is sufficiently compressed to provide high levels of divertor radiation whilst maintaining good plasma performance, but that for Ne, the impurity is not well retained in the divertor and plasma performance is impaired, due in large part to its effect on the pedestal and the consequent changes in seeded impurity and tungsten transport.

Experiments in the JET-ILW [74] similarly find good performance with N, with increased pedestal temperature compared with otherwise identical unseeded discharges and efficient divertor radiation, but with dependencies on divertor geometry (horizontal versus vertical outer target). At the same input power, Ne radiates less in the divertor, degrades pedestal pressure and requires considerably higher input power than N-seeding simply to maintain unseeded pressures. With insufficient power, pedestal radiated power losses are too high and the plasma operates too close to the H–L power transition threshold, with reduced confinement and transitions to and from H-mode. In both ASDEX Upgrade and JET, N-seeding at high enough levels leads to

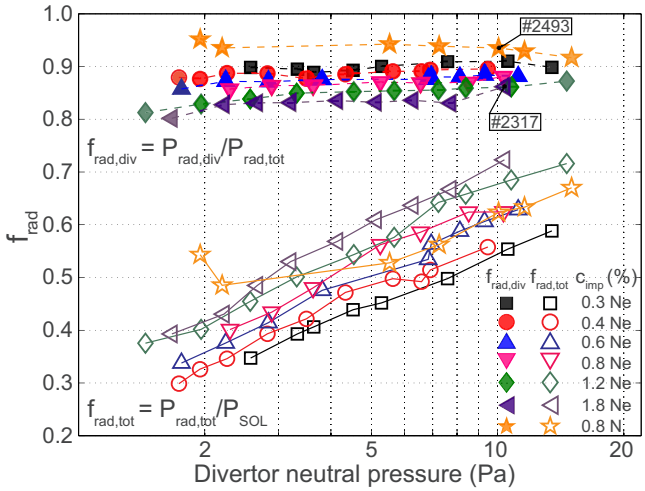

Fig. 8. Neutral pressure dependence of the total and divertor radiation fractions for the SOLPS-4.3 database simulations in Fig. 5 at P_{SOL} = 100 MW. The 2-D divertor radiation distributions in Fig. 9 correspond to the pair of cases marked at high p_n.

significant radiation from the X-point region and is associated with partial to full detachment at the outboard target (and complete detachment at the inner target). These results may be contrasted with those found on radiative divertor experiments on Alcator C-Mod with molybdenum PFCs at high magnetic field in which, for both N and Ne seeding in the ELM-free "EDA" mode, partially detached divertor conditions at normalized confinement (H_{98} ~1) with edge power flows only marginally above the H-mode threshold power (by factors of 1–1.4), as in ITER, were achieved [75]. Here, as in the JET and ASDEX Upgrade experiments, at high radiative fractions, the radiation is observed to occur mostly in the X-point region, with some incursion onto flux surfaces just inside the separatrix. Apparently, in C-Mod, this was insufficient to strongly affect the pedestal top, even in the case of Ne.

In ITER, the SOLPS-4.3 simulation database, though still sparse for N, indicates that for both N and Ne, the impurity radiation is well confined to the divertor across the operating range in p_n and c_{imp} explored thus far. Fig. 8 provides the dependence on p_n of the fractions $f_{rad,tot} = P_{rad,tot}/P_{SOL}$ and $f_{rad,div} = P_{rad,div}/P_{rad,tot}$ for the Ne-seeded database and for a single N series with c_N = 0.8%.

Here $P_{rad,tot}$ is the total power radiated in the simulation domain and $P_{rad,div}$ the power radiated in all computational cells below the vertical position of the X-point. These radiated powers include all contributors: impurity ions, neutrals (impurities and fuel, including molecules) and even Bremsstrahlung.

Several key observations may be drawn from Fig. 8:

- for all c_{imp}, $f_{rad,tot}$ increases monotonically with p_n, reaching ~0.70 (70 MW since P_{SOL} = 100 MW) at the highest p_n;
- $f_{rad,tot}$ increases with increasing c_{imp} at fixed p_n;
- $f_{rad,div}$ decreases with increasing c_{imp} (Ne only since database too restricted in N) and remains approximately constant with increasing p_n;
- $f_{rad,div}$ is within 0.8–0.9 for the range of c_{Ne}, being lower for higher c_{Ne} and approximately constant with p_n;
- N radiates more efficiently in the divertor than Ne for the same c_{imp};

Fig. 9 compares the 2D radiation distributions in the divertor region for the two specific simulations marked in Fig. 8, chosen for their close proximity in p_n and c_{imp} (both at c_{imp} = 0.8%) but differing in seeding species. The two cases had impurity and fuel gas puffs of 2.1×10^{20} Ne s^{-1}/1.85×10^{23} D s^{-1} (#2317) and 6.0×10^{20} N s^{-1}/1.74×10^{23} D s^{-1} (#2463) giving seeding/fuelling ratios of 1.1% and

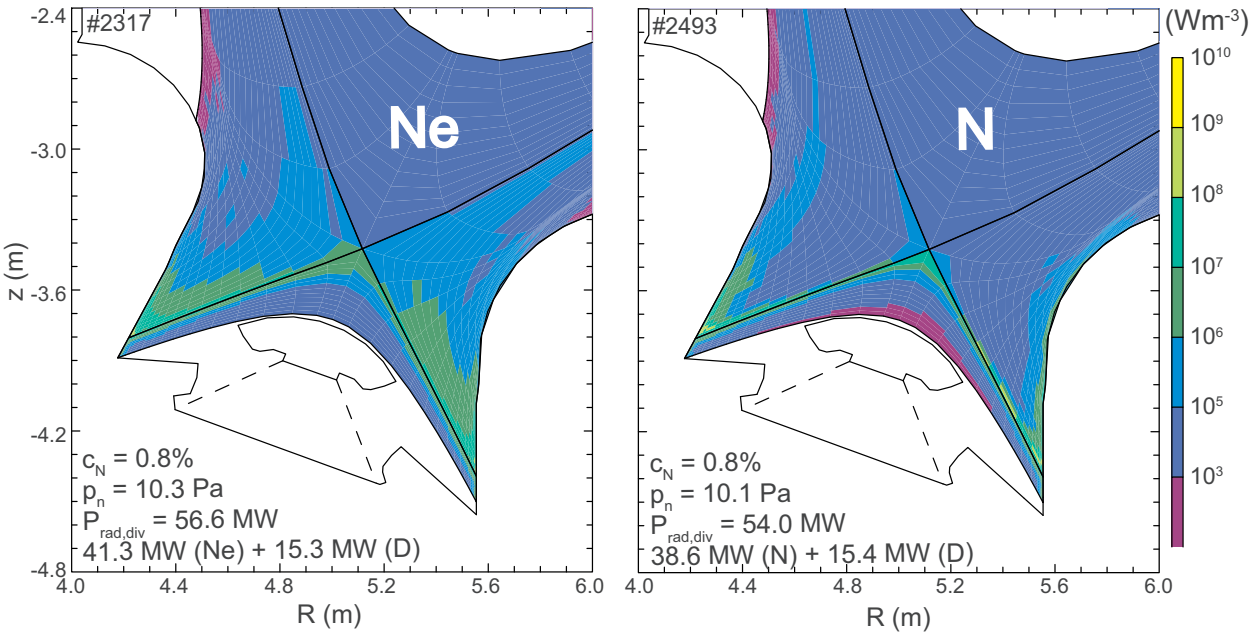

Fig. 9. Distributions of total radiation in the divertor for Ne (left) and N (right) seeding at P_{SOL} = 100 MW, high p_n ~10 Pa and similar $P_{rad,div}$, c_{cimp} (see Fig. 8 for the location of the cases in the main database). Whilst most of the radiation is localized to the divertor, the higher spread in the Ne case is clear.

2.4% respectively when both gas puffs are compared in terms of electrons s^{-1} (both have the same core source of D^+ (9.1×10^{21} s^{-1}), see Section 3.1.1).

These two cases are in fact very close to the "detachment limit" defined for these ITER studies (see Section 3.1.3) and are selected for their very high radiation fractions. In fact, the fuel throughput used in the simulations is higher than the stationary capability of the ITER pumping system which is limited to 200 Pa m^3 s^{-1} ($\sim 1 \times 10^{23}$ atoms s^{-1}). This is not a major issue since it is p_n and not throughput which determines the divertor operation. Essentially the same operational parameters (except He exhaust) could be recovered in the code by reducing throughput and pumping speed.

The runs have very similar $P_{rad,div}$ (~55 MW) with almost identical contribution (~15 MW) to the radiation from fuel excitation (originating from the hydrogenic components, including molecules). For both the radiation is strongly localized in the strike point vicinity, though the Ne distribution is clearly more extended, as would be expected from differences in ionization potential of the various charge states given that the distribution of plasma temperature is similar for both cases (not shown). The radiation is also very symmetric in both inner and outer divertors for both species, as might be anticipated from the rather symmetric target power loading seen at high p_n (see Fig. 5a). As a crude measure of impurity compression, the ratio $n_{imp,osp}/n_{imp,omp}$ of the impurity ion densities at the outer strike point and the outer midplane in the two cases is ~100 for N and ~30 for Ne. In fact, for the Ne-seeded cases, which represent the majority of the simulation database, this value of $n_{imp,osp}/n_{imp,omp}$ ~30 for run #2317 in Fig. 9 at p_n ~10 Pa is about as high as it gets. Except at very low p_n, where the compression is very poor, $n_{imp,osp}/n_{imp,omp}$ is generally in the range 10–20.

Regarding the ratio of impurity concentrations from downstream to upstream (the enrichment), $c_{imp,osp}/c_{imp,omp}$, this ranges from near zero to near unity with increasing p_n and is thus inconsistent with simple models (e.g. the well-known Lengyel model [76] which generally assume c_{imp} = constant along a given flux tube). A detailed comparison with Lengyel for the case of Ne-seeding [77] in fact finds that the simple model is conservative in comparison with the SOLPS database and predicts c_{imp} in the range 4–10 times higher at the point of ion flux rollover at the OT (see also Section 3.2.2).

On the basis of this comparison, it would seem that both N and Ne would be acceptable divertor radiators for ITER, unlike in most current devices with metal PFCs. This question has also been discussed in a companion paper [78] through the medium of a pure simulation study using the SOLPS-ITER code in which the behaviour of N and Ne seeded H-modes on ASDEX Upgrade and ITER (both characterized by vertical target configurations) is examined. The study differs from that of the SOLPS-4.3 database in having drifts activated and including an H-mode pedestal region (see also Section 3.2.2). In the case of ITER, the inclusion of drifts does not radically change the distribution of radiation nor the target loading found in SOLPS-4.3 for either N or Ne at the higher values of p_n (where operation at high performance is most likely), as might be expected given the high toroidal field in ITER and hence the lower drift strength.

On ASDEX Upgrade, drifts are in contrast seen to have a very strong impact on the HFS divertor region, cooling the plasma and increasing the impurity concentration there. As proposed in detail in [79] (from which the ASDEX Upgrade part of the study in [78] was extracted), leakage of impurities to the main chamber SOL can then occur with more or less efficiency via frictional coupling to the main ion flows depending on the location of the ionization position of the impurity with respect to that of the fuel and of the poloidal stagnation point of the flow velocity. This leakage efficiency is higher for Ne than N because the former ionizes further from the target than the main ions, whilst the latter ionizes closer. However, even though Ne spreads more widely than N in ITER, the large physical size of the divertor and the high divertor plasma temperature means that the majority of ion charge states responsible for the bulk of the radiation (the most powerful radiators are $N^{2+\rightarrow 4+}$ and $Ne^{3+\rightarrow 6+}$) remain well within the divertor volume for both species.

From the point of view of the pure simulation study at least (thus not necessarily born out experimentally), a second key effect appears to be the relative screening efficiency of the divertor SOL for fuel and impurities recycling at the divertor targets. In the ASDEX Upgrade case, neutrals more easily penetrate into the PFR region and can then fuel the divertor SOL along the poloidal length of the divertor legs, reducing the plasma temperature and modifying in turn the spatial locations at which the majority of the power is radiated. For the ITER simulation, where the SOL heat flux channel width is larger (fixed by the cross-field transport assumptions in the model), ionization of fuel and impurity

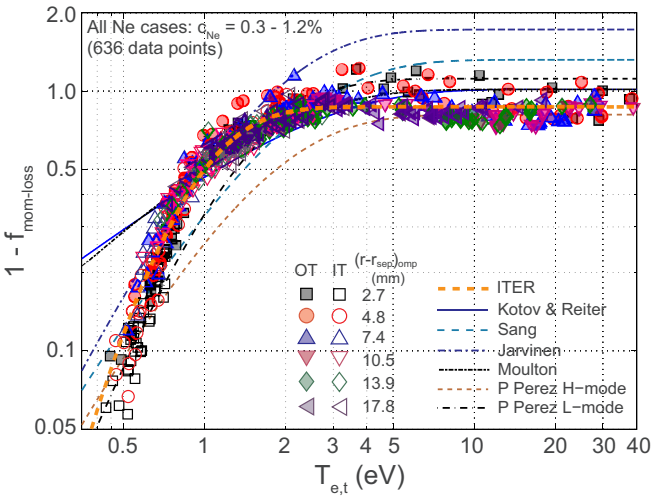

Fig. 10. Dependence of the upstream to target total pressure ratio on $T_{e,t}$ for the 53 SOLPS-4.3 Ne-seeded simulation cases at P_{SOL} = 100 MW in Fig. 5, for both IT and OT and for all flux tubes in the simulation within 2 mm ≤ $(r - r_{sep})_{omp}$ ≤ 18 mm. The best fit to the data according to the function in [69] is included (see main text), together with the selection of curves from similar modelling studies on different devices compiled in Fig. 15 of [69]. Note that unlike in previous figures, the colour and symbol coding now refers to radial position in the SOL with respect to the omp separatrix and not to c_{Ne}.

atoms occurs primarily in the divertor SOL, close to the target, keeping T_e high further upstream. This in turn means that the different impurity charge states exist closer to the targets in ITER and the radiation is better confined at both inner and outer targets. Further simulations are planned to study the consequences of reduced λ_q on this screening in ITER.

Although some impurity does of course still penetrate to the main chamber SOL and core regions (with Ne doing so more efficiently than N), on ITER T_e in the core region is high enough that Ne is fully stripped and cannot radiate. On ASDEX Upgrade, the highest charge states which exist in the pedestal region are not fully stripped and their radiative losses can be significant, offering an explanation for the more pronounced effect on plasma performance. The core-edge integration study in [3] showed that the same Q_{DT} can be obtained for both radiators, with obvious restrictions on the maximum allowed core impurity concentration (lower for Ne than N).

3.1.5. Momentum losses

Section 3.1.3 discussed the dependence of the target heat loading with varying fuel throughput and impurity seeding, showing the classical evolution of partial detachment for vertical target configurations with increasing levels of dissipation. Fig. 7 illustrated the progressive reduction in $p_{tot,t}/p_{tot,u}$ with increasing p_n for one specific value of c_{Ne} in the Ne seeded database. Fig. 10 now extends this to the entire Ne simulation set, but now plotting the pressure ratio on each flux surface of the numerical grid outside the separatrix within the first 2 cm of the omp SOL as a function of $T_{e,t}$ on that flux surface at both the IT and OT, excluding the first SOL ring outside the separatrix (at $(r-r_{sep})_{omp}$ = 1.2 mm) where radial diffusion into the PFR is strongest. There is a very clear and tight link, for all radial locations within the near to mid-SOL, between the total pressure-momentum losses and $T_{e,t}$, a correlation first identified experimentally for electron pressure loss in L-mode plasmas on the C-Mod tokamak [80] and very recently highlighted as a fundamental observation in both experimental and boundary code studies [69]. The latter review defines the "momentum loss factor", $f_{mom-loss} = 1 - p_{tot,t}/p_{tot,u}$ and shows how the trend seen in Fig. 10 for ITER is found in all code studies of this type for a variety of different divertor geometries and operating conditions. In the case of the ITER simulations, loss of total pressure on near-to-mid-SOL flux tubes begins at $T_{e,t}$ ~2 eV, falling gradually to values of $1 - f_{mom-loss}$ ~ 0.5 at $T_{e,t}$ ~ 1 eV and thereafter decreasing rapidly to $1 - f_{mom-loss}$ ~ 0.05 at $T_{e,t}$ ~0.5 eV, the lowest values achieved in the simulations and the range of $T_{e,t}$ over which volume recombination is expected to play a role in ion removal.

The arbitrarily chosen analytic form: $1 - f_{mom-loss} = A\left(1 - e^{-T_{e,t}/T^*}\right)^n$ with coefficients A, T* and n, is shown in [69] to reproduce well the shape of the pressure loss fraction vs. $T_{e,t}$ curves for the range of modelling and experimental studies considered there. These fits (modelling cases only), reproduced from Fig. 15 in [69] have been included on the ITER simulation data in Fig. 10 for comparison, along with a best (non-linear least squares) fit of the above expression to the ITER points across the whole span of $T_{e,t}$ (for which A = 0.87, T* = 0.43, n = 5.30 and the goodness of fit parameter R^2 = 0.96). Evidently, the ITER dataset can also be well represented by this trial function.

As first shown in [81] and discussed further in [69] in the context of a wider range of modelling studies, the explanation for the strong correlation between momentum-pressure loss and $T_{e,t}$ must in large part be attributable to neutral flux amplification at the targets – the number of collisions a neutral atom produced either by ion recombination at the surface or volume recombination (VR) experiences with the target surface before being re-ionized or lost from the system – originally defined in [82]. This amplification is itself strongly dependent on the molecular density, $n_{D2,t}$ of fuel particles right in front of the target (the only place where they can exist in the plasma), so that a correlation would be expected, and is found in modelling studies, between $n_{D2,t}$ and $T_{e,t}$ [69,81,83]. Fig. 11 shows that a similar trend is found in the ITER simulation database, over the same radial extent of the SOL as for the momentum losses in Fig. 10 (1 ≤ $(r-r_{sep})_{omp}$ ≤ 18 mm) and for both targets. A fit of the function $T_{e,t} = Bn_{D2,t}^{\beta}$ to all data with $T_{e,t}$ ≤ 10 eV yields B = 4.97 × 10^{13} and β = -0.66 for R^2 = 0.93, thus similar to the coefficients β found for a large variety of code studies in [69,81]. A fit of the same quality is obtained whether or not the first 2–3 flux tubes outside the separatrix are included (where diffusion into the PFR is strongest), but if all points above $T_{e,t}$ = 10 eV are also used, the data deviate very significantly from the fit. A potentially important caveat here, however, is that the SOLPS-4.3 simulations have been performed assuming a Be coated divertor target (see Section 3.1.1), which has ~6x

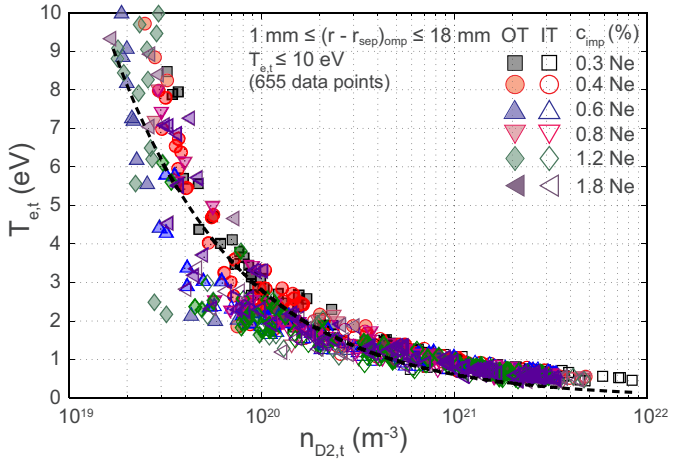

Fig. 11. Dependence of $T_{e,t}$ on the deuterium molecular density right in front of the target for the IT and OT, for all flux tubes with 1 mm ≤ $(r - r_{sep})_{omp}$ ≤ 18 mm (not identified individually) and for $T_{e,t}$ ≤ 10 eV. All 53 SOLPS-4.3 simulation cases at P_{SOL} = 100 MW in Fig. 5 are included. The dashed line is the best fit to the function $T_{e,t} = Bn_{D2,t}^{\beta}$ (see main text). This curve may be compared with those in Fig. 16 of [69].

lower energy reflection coefficient for atomic deuterium than W [84] and behaves very similarly to carbon, for which the code results discussed in [69,81] have been obtained.

In this context, a study has been performed [54] with SOLPS-ITER in which, for two example cases in the SOLPS-4.3 database (at low and high p_n), a fully Be-coated divertor is compared with the other extreme, a pure W target (but in neither case is target sputtering switched on). The principal differences appear indeed to be in the ratio of molecules to atoms in the target recycling flux (higher for Be), determined by the reflection and recombination properties of the different materials, which increases the molecular density in the divertor region for Be surfaces compared with W. However, the combined effect of the different contributions to the total pressure loss from atoms and molecules is such that for a given flux tube, the total loss is only slightly impacted by the material choice. The consequence is that the same degree of pressure loss is found at a slightly lower target plasma electron temperature for Be than in the case of a W target. The differences are, however, are small in comparison, for example, to the impact of impurity seeding.

It is thus clear that the ITER SOLPS-4.3 simulations find similar trends in momentum loss as those seen in smaller devices and with very different divertor configurations. What drives the strength of the correlation between $T_{e,t}$, $1 - f_{mom\text{-}loss}$ and $n_{D2,t}$ remains to be identified. The 2-point model formatting (2PMF) analysis in [81] which used an extensive SOLPS-5.0 simulation dataset from the simulations of a series of slot divertor configurations, found as strong a link between volumetric power losses and $T_{e,t}$ as that between $T_{e,t}$ and $n_{D2,t}$. The fact that most of the power dissipation in the ITER simulations proceeds through seeded impurity radiation rather than from the deuterium atomic and molecular radiation (see e.g. Fig. 9), supports volumetric power losses as a key physical process required to obtain low $T_{e,t}$.

As for VR, which becomes very significant for $T_e \lesssim 1$ eV and which therefore might be expected to be playing a major role in the rapid decrease of $1 - f_{mom\text{-}loss}$ at low $T_{e,t}$ (Fig. 10), new "balance analysis" is underway in which the different contributions to particle and energy losses in any given flux tube in the code results are examined in detail. This capability, recently introduced into the SOLPS-ITER code version, can only currently be performed on output from that version so that new cases, equivalent to the SOLPS-4.3 runs, need to be generated. A series of such cases covering the range of p_n and c_{Ne} encompassed by the SOLPS-4.3 database is in preparation, using the same physics model in SOLPS-ITER as that used in SOLPS-4.3 to generate the main database. Preliminary analysis of the available converged new runs at high p_n indicates that the VR is more important at the inner divertor than the outer; for example, in a simulation for $p_n \sim 10$ Pa, integrating along the 3rd SOL flux ring outside the separatrix (corresponding to $q_{\perp,\,pk}$ at the outer target), the VR sink in the outer divertor is ~20% of the outer divertor particle source, while the VR sink in the inner divertor is ~80% of the inner source. Further analysis of more simulation runs is required, and is planned, including the application of the 2PMF approach proposed in [69] and a sensitivity scan where VR is turned off.

Ultimately, the hope is that reduced models, along the lines advocated in [69], might be used to generate solutions for ITER, based on SOLPS-4.3 and forthcoming SOLPS-ITER simulations. This would naturally provide a much more computationally rapid framework suitable for inclusion in integrated models of the ITER plasma which require simpler descriptions of the divertor response than obtained with full plasma boundary code runs, but which must capture the essential (at least two-dimensional) physics at play. Such reduced models need data such as those shown in Figs. 10 and 11. This of course represents a different approach to the scalings which have been developed on the basis of the global simulation database for use as input to core modelling and which have constituted the mainstay of integrated modelling for the ITER divertor thus far. The advantage is a framework which might be more generally applicable to a wider range of conditions.

3.2. Factors influencing the peak power flux density

The p_n vs. $q_{\perp,pk}^{sym}$ operating window in Fig. 5a is the most sophisticated prediction for the ITER divertor power handling performance currently available, but is nevertheless incomplete in the sense that several additional factors will modify (and indeed unfortunately usually increase) the simulated peak heat flux densities. This section will examine most of the key such factors, beginning (Sections 3.2.1 and 3.2.2) with the case of the unperturbed magnetic equilibrium which has been the focus of the paper thus far. Section 3.2.3 will consider the issue of target loading during the application of 3-D fields for ELM control/suppression which may eventually turn out to be the standard operating mode for ITER at high performance, but for which divertor plasma simulations are still in their relative infancy compared with the 2-D axisymmetric situation.

3.2.1. Component shaping

The first and easiest factor to account for which impacts the SOLPS-4.3 predicted values of $q_{\perp,pk}^{sym}$ is the geometrical contribution due to divertor target tilting and MB surface shaping (see Fig. 2 in [36] for a schematic description of these geometrical factors). The former has always been recognized as necessary to protect against the macroscopic (several mm) radial misalignments which are expected to occur between neighbouring divertor cassettes (with design toroidal separation of 20 mm) due to assembly tolerances during installation in the vacuum vessel [38]. Regarding the latter, the question of whether or not potential radial misalignments (maximum specified value 0.3 mm) between the toroidally neighbouring individual W MB chains (plasma-facing units, PFU) comprising the IT and OT need to be protected by shaping has been the subject of significant R&D in recent years as the IO has sought to freeze the final divertor design [36].

The most straightforward solution is the use of a toroidal bevel on the MB top surface, with bevel height of 0.5 mm to protect the worst case misalignment with some margin. As shown by the very detailed numerical ion orbit study in [37], itself benchmarked against state-of-the-art particle-in-cell simulations [85], this eliminates the problem of steady state poloidal gap (PG) edge loading and mitigates a substantial component of the ELM PG heat loads. Elimination of the stationary PG loading comes at the price of an increased field line incidence angle at the MB surface. The combination of the global target tilt angle (~0.5°) and the MB toroidal bevel (with bevel angle = 1.0°) required to protect (with margin) a 0.3 mm radial step between toroidally adjacent MBs, increases the field line incidence angle by 1.5° (see Fig. 3). This makes for rather steep total incidence angles, > 4° at the IT and OT strike points, increasing the surface power density due to the thermal plasma and plate ion recombination components of the total heat load (see below and Fig. 12) by a factor ~50% compared with the cylindrically symmetric target assumed in the SOLPS modelling.

The MB geometry, comprising a square block with a circular cooling channel naturally leads to a surface temperature at the toroidal extremities of the MB surface higher than that at the centre. Adding a toroidal bevel enhances this disparity on the magnetically wetted extremity. However, the increase is considered less problematic than the very severe PG edge melting which would almost certainly occur during even mitigated ELMs on ITER [37], or the very high stationary temperatures which would be reached during steady state loading of an unprotected edge [36].

Unfortunately, the toroidal bevel does not solve the problem of extremely localized overheating on the edges of the toroidal gaps (TG) running down the long dimension of the MB in the toroidal direction (see Fig. 1), both during ELMs and in steady state, or the "optical hotspots" on poloidal edges caused by particles able to penetrate down the TGs. For the OT, because both ions and electrons strike the upper edges of the MBs, the TG (and simultaneously the optical hotspot) steady state loading can be eliminated and ELM-induced loading

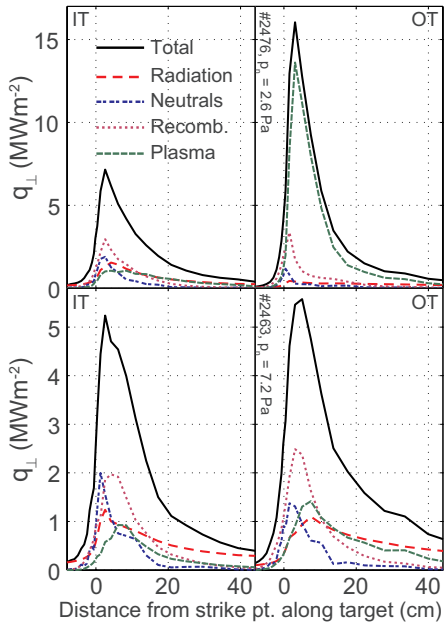

Fig. 12. Profiles of the different contributors to $q_{\perp}$ at the IT (left) and OT (right) for the two simulation cases identified in Fig. 5 a at low (upper) and high (lower) p_n. Here "Recomb." refers to ion recombination at the plate (which also includes a contribution from D atom recombination to D_2 molecules), "Plasma" to the contribution brought by thermal plasma to the plate "Radiation" to photonic loading and "Neutrals" to the power deposited mostly by CX neutrals. Note that the power flux densities do not account for target tilting and component shaping.

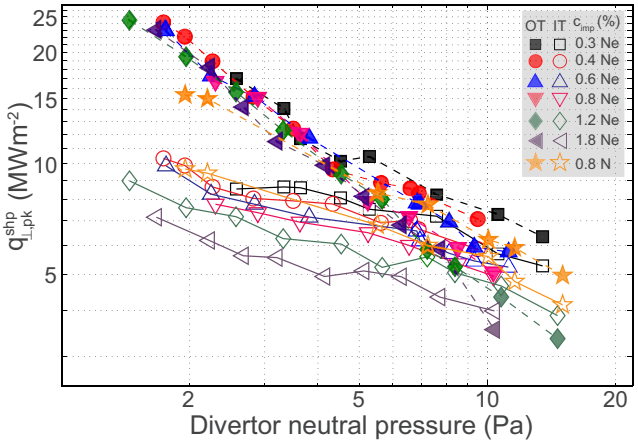

Fig. 13. Replot of Fig. 5a for peak target heat flux density vs. p_n, but with target tilting and MB toroidal bevelling taken into account (total incidence angle 4.7° IT, 4.2° OT, see Fig. 3). The correction to the projected fluxes affects only the plasma thermal flux and plate recombination components (see Fig. 12).

reduced by ~factor 2 with almost no further penalty on surface power density by implementing a "shallow" planar toroidal-poloidal bevel [86]. At the IT, the inclination of the magnetic flux surfaces means that electrons strike the upper and ions the lower MB edges and there is no shaping solution which can protect both [87]. Moreover, even at the OT, the shallow poloidal-toroidal bevel may only be used under the condition that MBs on toroidally neighbouring PFUs be well aligned poloidally. This is considered unfeasible from the engineering point of view.

A deeper poloidal bevel would be immune to PFU poloidal misalignments and, in the case of ELMs, reduces further the upper TG loading, at the expense of slightly increased lower TG heating [86]. However, the deep bevel would yield ~30% higher stationary loads due to thermal plasma and ion recombination on the MB surface compared with the toroidal bevel alone (thus a factor ~2 higher than a non-shaped surface). This is of particular concern in cases in which the divertor may transiently reattach (corresponding to lower p_n) when the out-in $q_{\perp,pk}$ asymmetry and the OT loads increase rapidly (see Figs. 5a and 13). Given that both TG edges cannot in any case be protected at the IT, the increased stationary loading at the OT due to the addition of the deep poloidal bevel is considered prohibitive. In view of all the above considerations, it has been decided to implement only a toroidal bevel on the top surfaces of MBs in the high heat flux areas (straight portions) of the vertical targets. This decision consciously acknowledges that melting of TG edges (Section 5) and at optical hotspots may have to be accepted at both targets. Further experimental work and modelling is required to evaluate the consequences for the MB lifetime.

The inclusion of a toroidal bevel naturally introduces a magnetically shadowed region on the surface of each MB which cannot be accessed by thermal plasma loads. As shown in Fig. 12, where profiles of the principal contributors to the total target heat loading for two of the Ne seeded cases at fixed c_{Ne} = 1.2% in the $q^{sym}_{\perp,pk}$ vs. p_n domain of Fig. 5a are compiled, the shadowed region (amounting to between 5% and 40% of the total MB surface area for the baseline q_{95} = 3 magnetic equilibrium depending on the magnitude of the radial misalignment between toroidally neighbouring MBs [37]) has varying impact depending on the operating point and on the target location (IT or OT). At low p_n the thermal plasma contribution completely dominates at the OT (where the plasma is in the high recycling regime near the strike point – see the T_e profile in Fig. 6b for p_n = 2.6 Pa), accounting for almost the entire surface heat load. The strong out-in asymmetry (Fig. 5a and discussion in Section 3.1.3) at low pressure means that the IT is already in a partially detached state, so that the combined contributions of ion recombination at the plate, CX neutral impact and photonic radiation dominate over the thermal plasma contribution in the strike point regions.

At higher p_n, the target heat load densities symmetrize and both strike point regions are strongly detached, with relatively low contribution of thermal plasma to the target loading. Since charged particles deliver the thermal plasma and plate ion recombination components to the target, the magnitude of their contribution is sensitive to total magnetic field incidence angle, whilst the CX and photonic loading contributions are normal to the plate surface and are unaffected by magnetic shadowing. This has the important consequence that the impact of MB front surface shaping is reduced when operating in a more detached state (namely high p_n).

Taking proper account of the shaping for the adopted design values of the toroidal bevel applied to MBs in the high heat flux areas and including the global target tilting, generates a corrected version of the p_n vs. $q^{sym}_{\perp,pk}$ operating curve in Fig. 5a, where now the variable $q^{shp}_{\perp,pk}$ denotes that shaping is taken into account. Fig. 13 gives the result, showing, as expected, much larger peak heat flux densities at low throughput (low p_n), but very similar values for more detached operating points, where the shaping has much lower impact. The different detachment states at the two targets at low p_n means that the inclusion of shaping increases the out-in asymmetry compared to the cylindrically symmetric case (i.e. the situation with no MB surface shaping or target tilting). The overall effect is to shift the acceptable operating point in terms of target power handling to higher p_n. What precisely "acceptable" means will be further discussed in Section 4.

In the case of operation at higher q_{95}, corresponding to the lower I_p advanced scenario plasmas foreseen in the latter stages of the FPO campaign (Section 2), field line incidence angles, and hence plasma wetted areas will decrease to values which could be as little ~35% of the total MB top surface area, depending on the relative radial misalignments of neighbouring blocks. Unpublished data from electron beam testing of MBs down to 25% partial loading at up to 20 MW m^{-2} performed under contract to the IO shows that the thermal performance

is maintained and there are no adverse consequences for the MB integrity.

3.2.2. Narrow heat flux channels and drifts

Considering still the case of an unperturbed magnetic equilibrium, there are two further factors which may influence the target heat loading in addition to component shaping: heat flux channel width and fluid drifts. Beginning with the former, Section 3.1.1 has discussed how empirical scaling on current devices and ion magnetic drift theory for the upstream heat flux width extrapolate to $\lambda_q \sim 1$ mm for the ITER burning plasma baseline at $I_p = 15$ MA. Turbulence simulations using the XGC1 and BOUT++ codes find, in contrast, that the ion orbit prediction is broken at the ITER scale and that $\lambda_q \sim 5$–6 mm might be expected, closer to the $\lambda_q \sim 3.5$ mm fixed in the SOLPS-4.3 database (Fig. 4).

To examine the consequences for power handling of a much lower λ_q, cross-field transport coefficients can be reduced in the ITER SOLPS modelling. This numerically challenging exercise is being attempted at the time of writing with the new SOLPS-ITER code, for the W/Be environment, but the results are insufficiently mature to be presented here. Instead, recourse can be made to an earlier SOLPS-4.3 study (thus no drifts) made for the case of carbon divertor plates and $P_{SOL} = 100$ MW [28]. In that work, fuelling throughput scans were performed on a grid with finer resolution close to the separatrix, and with $D_\perp$ and $\chi_\perp$ reduced to 50% and 25% of the standard values ($D_\perp = 0.3$ m^2 s^{-1}, $\chi_\perp = 1.0$ m^2 s^{-1}, Section 3.1.1). A subset of the results reported in [28] have been extracted for comparison with the SOLPS-4.3 "carbon-free" database, focussing on $q_{\perp,pk}^{shp}$, and are shown in Fig. 14, which is a replot of Fig. 13 (note the extended *y*-axis) and which also includes some new points obtained from SOLPS-ITER drift runs (see below).

From the "reduced-transport" carbon SOLPS-4.3 runs, the fuel throughput scan at $D_\perp = 0.075$ m^2 s^{-1}, $\chi_\perp = 0.25$ m^2 s^{-1} (baseline reduced by a factor 4, denoted by $f_{perp} = 0.25$ in Fig. 14) has been included for both IT and OT, along with the case for standard $D_\perp$ and $\chi_\perp$ for the OT only (to avoid too much clutter on the plot), showing how $q_{\perp,pk}^{shp}$ for carbon is actually quite close to the metal wall impurity seeded results and justifying the use of data from a "natural" seed impurity produced by chemical and physical erosion at the targets. For these two series the average separatrix impurity concentration (defined in the same way as c_{Ne} – see Fig. 3) is $c_C = 1.48\%$, at $f_{perp} = 0.25$ and

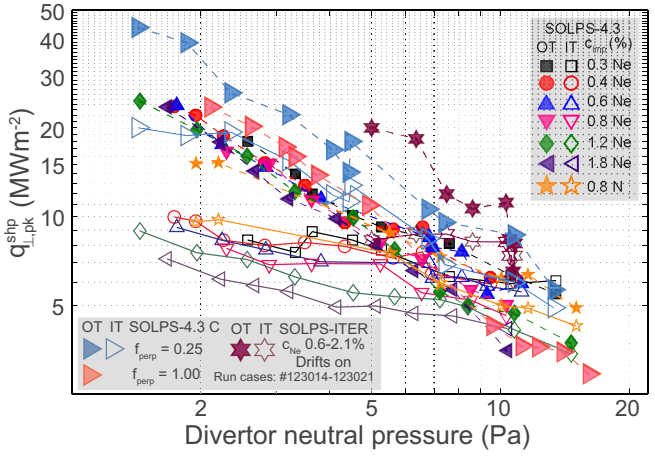

Fig. 14. Compilation of the SOLPS-4.3 $q_{\perp,pk}^{shp}$ vs. p_n operational space of Fig. 13 for Ne and N seeding with SOLPS-4.3 carbon cases at "standard SOL $D_\perp$ and $\chi_\perp$" ($f_{perp} = 1$, OT point only for clarity) and 4x reduced transport ($f_{perp} = 0.25$, see [28]) and new SOLPS-ITER cases with standard SOL transport but fluid drifts activated at full strength (see [90]). In all cases, $P_{SOL} = 100$ MW with target tilting and MB toroidal bevelling taken into account. Note the difference in the y-ordinate upper limit in comparison with Fig. 13.

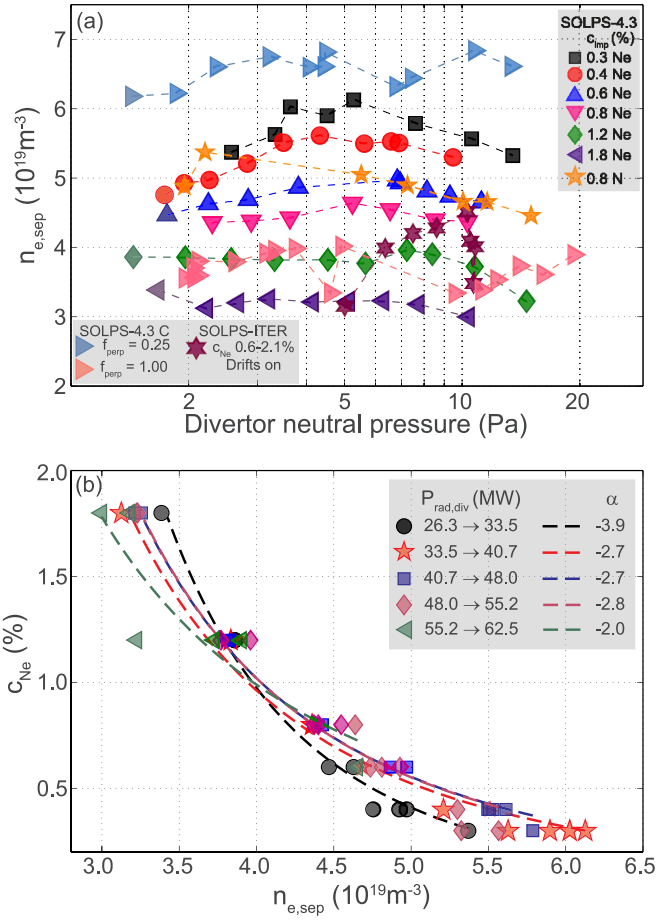

Fig. 15. (a) Dependence on p_n of $n_{e,sep}$ for the simulation cases of Fig. 14. (b) Variation of c_{imp} with $n_{e,sep}$ for the Ne-seeded data in (a) with the colour coding and symbols now representing groups of points with the $P_{rad,div}$ in the 5 intervals given in the legend. The dashed lines are fits of the function $c_{imp} = A n_{e,sep}^{\alpha}$ to each set of points within each band of $P_{rad,div}$ with the parameter α in each case given in the legend. Note that the colours and symbols used in (a) and (b) are completely unrelated.

$c_C = 1.41\%$ for standard transport ($f_{perp} = 1$). All points in Fig. 14, in common with Fig. 13, take proper account of the divertor target shaping. Following the same procedure described in Section 3.1.1 and Fig. 4, the reduced transport runs yield an upstream $\lambda_q = 1.3 \pm 0.2$ mm (c.f. 3.4 ± 0.5 mm for standard transport), quite close to the $\lambda_q \sim 1.0$ mm expected from the experimental scaling.

Reducing transport has the expected effect of increasing $q_{\perp,pk}^{shp}$ at given p_n, requiring operation at high p_n to maintain acceptable target peak heat loads. Note also that as the heat flux channel narrows, the out/in asymmetry weakens significantly, corresponding to less strong partial detachment at the IT. For p_n in the range of 10 Pa, $q_{\perp,pk}^{shp}$ remains manageable. As shown in detail in [28], the effect of reduced λ_q is much less pronounced at high p_n because there the heat flux reduction from X-point to target is primarily driven by radiation (mostly due to impurity) with much lower contributions to power removal from radial transport and direct neutral interaction. As the heat flux channel constricts, the higher density there provides higher P_{rad} ($\propto n_e^2$ at least – see Fig. 15(b)) and the increased radiation outweighs the reduction in radiating volume. Further out in the divertor SOL, the behaviour is practically unaffected by the reduced λ_q. At lower p_n, the contribution of radiation to power loss is weak so that target power deposition is dominated by charged particles and the impact of reducing transport is significant, producing values of $q_{\perp,pk}^{shp}$ at both IT and OT far beyond acceptable stationary loading. The consequence of the increased density in the separatrix region for the upstream density at high p_n is examined

below (Fig. 15a).

Drifts are well known in current devices to have a strong impact on stationary divertor power loading (see e.g. [67,88]). For forward B_φ operation, they tend to enhance the natural out/in target power asymmetry arising from toroidal geometry, though the actual peak heat flux density obtained depends of course on divertor plate geometry (this is also the case for the ITER divertor as noted in Section 3.1.3, with the steeper inclination angle of the IT). Computationally, the inclusion of drifts in ITER simulations is extremely challenging, and is possible within the SOLPS framework only for code versions 5.0 and above, of which SOLPS-ITER is the most up to date manifestation. Switching drifts on in the code leads to extremely long convergence times (years) for ITER burning plasmas and it has only been possible very recently, with the development of a suite of code speed-up schemes [89], to obtain a series of code runs corresponding to a modest subset of the SOLPS-4.3 database at $P_{SOL} = 100$ MW. The 8 points available at the time of writing are included in Fig. 14, discussed above in relation to the consequences of reduced transport (without drifts). The effect of target shaping has been fully accounted for. A detailed description of these code runs, deeper physics analysis and a discussion of the differences between these new simulations and their non-drift SOLPS-ITER and SOLPS-4.3 counterparts may be found in [90].

Apart from the activation of drifts, the new SOLPS-ITER simulations differ in an important aspect from those obtained with SOLPS-4.3: they include an H-mode transport barrier inside the separatrix, obtained by specifying radial profiles of $D_\perp$ and $\chi_\perp$ tuned to provide approximately the expected $Q_{DT} = 10$ pedestal profiles of n_e, T_e and T_i. Inclusion of the transport barrier is important given the impact on drifts of the strong electric potential gradients which develop in the H-mode. In the SOL, $D_\perp = 0.3\ m^2\ s^{-1}$, $\chi_\perp = 1.0\ m^2\ s^{-1}$ are fixed, as in the SOLPS-4.3 runs, producing a similar near SOL omp $\lambda_q \sim 4$ mm. Unlike the SOLPS-4.3 simulations, the SOLPS-ITER runs assume W at the divertor targets (see discussion in Section 3.1.1), though W impurity is not evolved. They also use Ne impurity seeding, but it has not yet been possible to produce a well-defined series of throughput scans at varying c_{Ne} as in the SOLPS-4.3 database. One or two equivalent N-seeded drift runs are available but are not included in Fig. 14 (see Section 3.1.4 and [78]).

The trend in the new runs is similar to the non-drift cases: with increasing p_n, the out-in asymmetry reduces. However, the asymmetry increases more markedly than the non-drift cases as p_n decreases, with $q_{\perp,pk}^{shp}$ at the OT rapidly exceeding tolerable limits. The tendency for the loads to symmetrize at high p_n is qualitatively expected with deepening detachment when the convective zone widens in the strike point region and drifts play a lesser role. As shown in [78], the divertor radiation distributions with and without drifts are very similar at the higher p_n for approximately equivalent c_{Ne}. What is clear is that if these new results can be trusted, they are a further indication that operation at higher p_n is likely to be required at ITER from the point of view of power handling. Drift runs at low SOL transport have not yet been attempted, but are planned and are clearly a necessary step.

An important question to address is the extent to which, in pushing to higher p_n and hence deeper detachment than covered in the existing ITER SOLPS-4.3 database, the radiation distribution moves towards the X-point, eventually forming an X-point MARFE, as seen commonly on current devices (see e.g. [73,74]) at high seeding rates. Here, apart from the impact of increased radiation inside the confinement region/pedestal, which may prevent strongly detached regimes on ITER given the proximity to the L–H power transition threshold at which the device will operate, a key issue is the stability of the detachment front. From the perspective of detachment control, it will be important to assess whether or not the sharp transitions/bifurcations ("detachment cliff") which have been observed experimentally in some current devices, may also appear on ITER at higher levels of dissipation than considered in the current database. In fact, recent modelling of the bifurcations seen on the DIII-D tokamak during H-mode operation with the UEDGE code can only qualitatively match experiment if drifts and currents are activated in the simulations [91].

As mentioned earlier, the studies reported in [28] with SOLPS-4.3 at reduced transport used a more refined grid in the separatrix region. This issue of grid resolution is a further factor which can influence $q_{\perp,pk}^{sym}$, even in the case of "normal" transport assumptions. A recent study of the impact of grid discretization error using SOLPS-4.3 found a ~25% increase in $q_{\perp,pk}^{sym}$ when the grid was refined by a factor 4 for partially detached, low power, D-only ITER "test" cases [92]. Further tests with SOLPS-ITER are underway at the time of writing for the full power, impurity seeded cases.

Recent work using a large database of measurements from the JET and ASDEX Upgrade tokamaks finds clear evidence, supported by quantitative arguments, for a central role of the upstream separatrix density normalized to the Greenwald density, $n_{e,sep}/n_{GW}$, in determining the onset of the H–L back transition [93]. This H-mode density limit is strongly correlated with the approach to the ideal ballooning instability threshold at the plasma edge. Fig. 15a gives the dependence of $n_{e,sep}$ (evaluated at the omp) on p_n for the simulation cases compiled in Fig. 14, thus including the reduced and "normal" transport carbon cases and the new SOLPS-ITER drift runs for W/Be.

An obvious immediate trend seen in Fig. 15a is the rather weak and, in some cases, absence of any dependence of $n_{e,sep}$ on p_n for given c_{imp}. A somewhat stronger dependence, $n_{e,sep} \propto p_n^{0.25–0.3}$, in the region around partial detachment has been reported in a recent paper from ASDEX Upgrade [94]. These observations (code and experiment) are consistent with a simple theoretical analysis [44] which relates the maximum upstream plasma pressure (and hence density) that the divertor can sustain with energy balance in this plasma. Fig. 15a is indirect evidence that the ITER divertor provides efficient neutral confinement within the range of p_n covered by the simulations. However, to show this quantitatively requires a complete study of particle balance in the system, comparing the neutral ionization rate in the main chamber SOL and divertor, properly accounting for the neutral recombination source in the divertor and the contributions of gas puffing and wall recycling in the SOL. This is not performed here and is left for future work.

Fig. 15a also clearly demonstrates that as c_{Ne} is reduced, $n_{e,sep}$ increases for given p_n. This is because as c_{Ne} increases, radiation increases and the power available for molecular dissociation and ionization/excitation of the fuel molecules/atoms decreases so that the upstream ion density and hence $n_{e,sep}$ decreases. It is also notable that for the carbon run series at standard transport, for which $c_C = 1.41\%$ on average for the throughput scan, the data for $n_{e,sep}$ lie roughly at the same values for the zero-carbon series at $c_{Ne} = 1.2\%$. There does not appear to be any attention paid in the experimental literature to the behaviour of $n_{e,sep}$ with c_{imp}, with most emphasis given to the effect on the H-mode pedestal (see e.g. [74]). This is most likely related to the difficulty of measuring $n_{e,sep}$ itself under the high power H-mode conditions in which most seeding work is performed on current devices.

The strong dependence of c_{imp} ($= c_{Ne}$) on $n_{e,sep}$ seen in Fig. 15a is examined further in Fig. 15b for the Ne-seeded simulations only, since this represents the largest dataset in which c_{imp} is systematically varied. Here the data are grouped according to their value of $P_{rad,div}$ within 5 bands of width ~7 MW and centred on 30, 37, 44, 52 and 59 MW, spanning the whole range of $P_{rad,div}$ (from 26.3 → 62.5 MW). A fit to the function $c_{Ne} = A n_{e,sep}^{\alpha}$ has been performed for the data in each of the 5 $P_{rad,div}$ intervals. Values of α range from -2.0 → -4.0, with the $n_{e,sep}^{-2}$ dependence found for the highest $P_{rad,div}$where detachment is strongest (i.e. at the highest p_n), and a scaling with $n_{e,sep}^{-4}$ at the lowest $P_{rad,div}$. The trends are thus in general stronger than expected from simple models, such as the Lengyel approach mentioned in Section 3.1.4 [76] , which give $c_{imp} \propto n_{e,sep}^{-2}$, but which assume $c_{imp} = cnst$ along a given flux surface. As discussed in [77], one possible explanation for the stronger dependence is increasing radial transport loss from the first SOL ring (where the c_{imp} metric is defined in this work, Section 3.1.1), which decreases with decreasing $n_{e,sep}$ so that the increase in c_{imp} required at

lower $n_{e,sep}$ to remove all the power conducted down the flux tube is higher than predicted than the Lengyel model. What the curves in Fig. 15b also provide is an explanation for the evident insensitivity of $q_{\perp,pk}^{sym}$, $q_{\perp,pk}^{shp}$ in Figs. 5a, 13 and 14 to c_{imp}, especially at low p_n, since $P_{rad,div} \propto c_{imp} n_{e,sep}^{-2}$. Although as yet unpublished, there is tantalizing new evidence from the ASDEX-Upgrade tokamak [95] that the behaviour predicted for ITER in Fig. 15b is actually found experimentally for N-seeded H-modes. If this is confirmed and found also in simulations of this device (such as those performed by Reimold et al. [96]), this would be an important confirmation of a principle finding for the ITER divertor operational space.

Returning to the question of maximum tolerable $n_{e,sep}$, the highest values in Fig. 15a for the "standard transport" assumption (namely for $\lambda_q \sim 3.5$ mm at the omp, Fig. 4) are found at the lowest c_{Ne} and peak at $n_{e,sep} \sim 6 \times 10^{19}$ m^{-3}. This is 0.5 n_{GW} for the 15 MA ITER baseline burning plasma ($n_{GW} = I_p/\pi a^2$ where the units are 10^{20} m^{-3}, MA, m). The analysis in [93], finds the observed H-mode operational boundary to be roughly limited by $n_{e,sep}/n_{GW} < 0.4$–0.5 in JET and ASDEX Upgrade, when the MHD ballooning parameter at the separatrix location reaches values in the range of theoretical predictions for ballooning instability. This observed critical $n_{e,sep}/n_{GW}$ can be quantitatively derived using the experimental λ_q scaling [56], itself obtained partly from JET and ASDEX Upgrade data. If the same limit also applies to ITER, then the lowest seeding values in the SOLPS-4.3 database would be marginal, though these were obtained for SOL transport assumptions giving higher λ_q than the empirical scaling. At reduced transport (the carbon case at $f_{perp} = 0.25$ in Fig. 15a), giving $\lambda_q = 1.3$ mm, closer to the empirical scaling prediction for ITER at 15 MA, $n_{e,sep}$ exceeds the predicted limit and H-mode operation may be compromised. Since the lower c_{Ne} are those at which Q_{DT} is maximized [3], a compromise will need to be sought for the appropriate seeding level, assuming Ne as extrinsic radiator and depending on the real λ_q which is found on ITER. What is clear is that more simulations are required, particularly at reduced transport in the W/Be environment with impurity seeding (Ne and N).

3.2.3. Impact of 3D fields

The entirety of this article has thus far been dedicated to the case of divertor performance in the case of an unperturbed magnetic equilibrium leading to axisymmetric target power loading, broken only by the inclusion of component shaping, which is easily accounted for by applying geometric (via modified field line incidence angles) projection to the fluxes predicted by 2-D SOLPS modelling. However, the ELMs found universally to accompany the baseline H-mode operation on which ITER relies to achieve its fusion performance goals will be too damaging to the divertor targets if they are not at the very least strongly mitigated and preferably completely suppressed (Section 5). The most promising current technique for ELM control/suppression is the application of external, symmetry breaking magnetic perturbations (MP) achieved using a variety of coils installed in-vessel and thus close to the plasma boundary (see e.g. [97–99]). On this basis, ITER is being equipped with an extensive set of such coils, located behind the first wall shielding blanket and comprising 3 toroidal rows of 9 window-frame type units [100].

The application of MP fields modifies the magnetic structure of the boundary plasma. This is a complex process and not all aspects are yet fully understood, specifically the precise mechanism driving ELM suppression. An important component is the impact of the MP field amplitudes on resonant surfaces inside the plasma. In a linear superposition of the MP field on the axisymmetric plasma equilibrium, magnetic islands formed on these resonant surfaces can overlap, yielding a stochastic magnetic field [101,102]. However, the plasma is a highly conductive medium and responds to the external magnetic field components. When ELM suppression is achieved, this is found to act like an ideal kink-peeling response, inducing an amplifying local kink mode on resonant surfaces in the plasma edge where the pressure gradient is high and the electron diamagnetic drift is low enough [98,103,104]. When this occurs, several of the magnetic islands will be suppressed due to plasma screening of the associated resonant field amplitudes and only the outermost modes will be strong enough to open a magnetic island, possibly driving the change in transport required to prevent the pedestal from reaching the peeling-ballooning threshold.

A second key phenomenon, better understood but still dependent for a full description on improved understanding of the internal plasma response, is the appearance of helical magnetic lobes created when the separatrix splits into two distinct branches (stable and unstable manifolds) as a result of the small radial non-axisymmetric perturbations to the axisymmetric equilibrium field [105]. These separatrix lobes break the axisymmetry of the plasma boundary and may intersect the divertor targets, producing helical magnetic footprints [102].

Simulation of these non-axisymmetric divertor conditions necessarily requires a 3-D model, with the only sufficiently mature contender presently available being the EMC3-Eirene code [106,107], which uses the same neutral kinetic code (Eirene) as that deployed in the SOLPS package, along with the Braginski fluid equation solver EMC3. However, until very recently, numerical oscillations arising under conditions of low divertor T_e and high n_e [108] have meant that the code could not access strongly dissipative conditions and its only major application to the prediction of ITER divertor power loads in the presence of MPs was restricted to moderate high recycling conditions [109]. This has now been resolved [110], at least with regard to dissipation involving fuel species, by introducing a linearization of the sink term in the electron energy balance equation arising from electron impact losses on particles of the neutral gas. The modified code has been benchmarked against a SOLPS-ITER low power ($P_{SOL} = 20$ MW), hydrogen only gas scan, finding clear particle flux roll-over and pronounced heat flux detachment in very good agreement with the 2-D code results and no oscillations in the solution.

It is now possible to improve upon some aspects of the initial EMC3-Eirene simulations for MP application on ITER at high performance reported in [109], though an improved impurity model is still lacking in the code to properly treat the case of the highly radiative divertor. A possible resolution to this deficiency is in fact now imminent following the implementation of a kinetic ion transport module in Eirene [111]. In addition, one of the authors of the present manuscript (H. Frerichs) is currently in the final stages of developing the capability to deal with volume recombination in EMC3-Eirene.

A first application of the code with improved treatment of particle detachment to ITER has been to examine the divertor target loads to be expected when MP fields are first applied to test ELM control in the initial non-nuclear (PFPO-1 – Section 2) phase of operation [112]. According to the IRP, such attempts will be made at $I_p = 5$ MA, $B_\varphi = 1.8$ T, allowing use of the baseline magnetic equilibrium at $q_{95} = 3$ and benefitting from the low toroidal field to allow H-mode access with the limited input power which is expected to be available at that point of ITER exploitation. Code runs have been performed for a pure hydrogen test case in which $P_{SOL} = 30$ MW and in which the standard SOLPS cross-field transport ($D_\perp = 0.3$ m^2 s^{-1}, $\chi_\perp = 1.0$ m^2 s^{-1}) has been applied.

To account for the plasma response features described briefly above, perturbed equilibria are provided by the MARS-F [113] linearized, resistive single fluid MHD code for the case of MP application with toroidal mode number $n = 3$ and in which the coil phasing (and hence the MP poloidal spectrum) has been optimized for ELM control according to the criterion of a maximized kink-peeling amplification near the separatrix mentioned earlier [114]. Variations in the level of plasma response, namely a dominantly screening response and a case with a clear level of resonant field amplification near the separatrix as a result of different magnitudes of toroidal rotation, have been used to explore two extreme plasma response cases as reference.

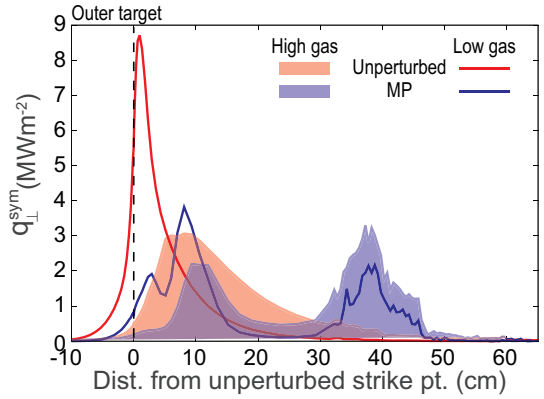

Fig. 16. Outer target heat flux density profiles (uncorrected for target tilting and MB shaping) at a toroidal angle of 60° from EMC3-Eirene simulations of a low power, pure hydrogen plasma with P_{SOL} = 30 MW, with and without n = 3 magnetic perturbation fields, at the low and high end of a gas puff scan from 1-9 × 10^{22} s^{-1}. The perturbed equilibrium is obtained with the MARS-F MHD code for optimized coil phasing at low toroidal rotation. The reference q_{95} = 3 SOLPS equilibrium corresponds to the non-perturbed case.

As shown in [112], although the calculated plasma response screens most of the resonances and produces a much reduced chaotic domain inside the separatrix in comparison to the vacuum field, resonant field amplification in the separatrix vicinity leads to large helical lobes in the SOL which can exceed the size of those obtained for the vacuum field approximation in the case of the largest assumed toroidal rotation. Some of these lobes intersect the targets, providing a pathway for plasma inside the separatrix to connect to the plate and presenting a potential problem for dissipation of the resulting heat flux given the high temperature of the plasma in the connected flux tubes.

Example EMC3-Eirene simulations are presented in Fig. 16, which compares the OT heat flux density (uncorrected for surface shaping, thus $q_\perp^{sym}$) at two points in the pure H gas puff scan in the range 1–9 × 10^{22} s^{-1} for an unperturbed equilibrium and for the case of MP application with coil phasing which produces an optimized (with respect to maximization of the kink-peeling amplification) plasma response at low toroidal rotation. The profiles are taken at φ = 60°, toroidally halfway through the 120° 3-D domain modelled for this n = 3 perturbation, and in the region where heat loads and radial extent of the lobes are highest. At all toroidal locations, the radial extent of the lobes is such that the 3-D heat flux pattern remains within the confines of the straight portions of the divertor targets where leading edges across poloidal gaps (see inset in Fig. 1) are protected by MB surface shaping (Section 3.2.1). At low gas puff rate, the unperturbed strike point is clearly attached, moving into a partially detached state at the highest gas injection rate in the scan (compare with the heat flux profile evolution in Fig. 6a for the burning plasma throughput scan at fixed impurity concentration).

In contrast, when MPs are applied, the heat flux pattern striates, with about a factor 4 reduction in power density at the original strike zone and two clear lobes appearing further out (centred at ~10 cm and ~40 cm from the unperturbed strike point in Fig. 16). The peak $q_\perp^{sym}$ is lower than the unperturbed case at both of these lobes, but crucially, when gas puff is increased, the first lobe partially detaches (at a lower roll-over particle flux than for the non-perturbed case), but at the second, the heat load actually increases (the particle load, not shown in Fig. 16, also increases at this location). This behaviour is very reminiscent of observations first reported from EAST [115] for the case of n = 1 perturbations driven by Lower Hybrid Current Drive (and thus not by currents in external coils). There it was conjectured, as mentioned above, that the lobes further out in the divertor SOL are connected to regions deeper in the plasma, where temperatures are higher, so that the plasma at the targets is still in the sheath limited regime. In this case, the heat flux density would increase with increasing particle flux and the lobe would be harder to detach. At the highest gas puff rates attempted in the simulations thus far for the particular case in Fig. 16, detachment of the far SOL lobes was not achieved.

Analysis is currently underway to study the connection between upstream and downstream in these ITER non-active operation simulations, but the result in Fig. 16 clearly shows that decoupling of divertor characteristics may well occur even in the early phases of ELM control tests on ITER. How easy it might be to detach these striated structures is an important area for further R&D. Experiments on current devices are hampered by the fact that ELM suppression has not yet been experimentally found under the dissipative divertor conditions necessary for power handling (namely at higher plasma density). In cases of ELM mitigation only, several experiments have been conducted (see [116] for DIII-D and NSTX and [117] for ASDEX Upgrade), with contradictory results, even in the same device, regarding the possibility of detaching non-axisymmetric target structures. The EMC3-Eirene enhancements described above can now hopefully be more widely deployed in support of understanding the experimental findings on present devices. Meanwhile, the code will continue to be applied to ITER scenarios of increasing complexity, at higher power and with seeded impurities, for different plasma response models and toroidal mode numbers. It is finally worth noting that the ITER MP coil set can be readily used to toroidally rotate and hence spread the 3D perturbation across the divertor targets in the case of excessive non-axisymmetric heat loads driving local MB over-heating, subject to constraints on the rotation frequency due to fatigue cycling at the MB cooling channel interface [100].

4. New criterion for allowed peak heat flux density

The SOLPS analyses presented in Section 3 demonstrate an increasing trend, as more refinements are included in the physics model and component tilting/shaping are included, for the divertor operating point to shift to higher neutral pressures if $q_{\perp,pk}$ is to remain at acceptable levels. As briefly mentioned in Section 1, the issue of what is "acceptable" is a materials and technology dependent criterion. The oft quoted value of 10 MW m^{-2}, as the maximum tolerable stationary heat flux density for ITER divertor, was historically determined as acceptable for CFC-based and W MBs and adopted as the engineering qualification standard once the decision was taken to move to a full-W divertor [118,119]. The "ITER full tungsten divertor qualification programme", [119], launched in 2012, consists of a 2-stage technology development phase in which the two Domestic Agencies (DA) supplying the divertor vertical targets (OT (Japan) and IT (Europe)) first demonstrated fitness for purpose (through thermal loading tests), using small-scale mock-ups, of their proposed joining technologies of W MBs to the cooling tubes and of the MB to steel support leg attachment which is used to join the PFU to the vertical target steel support structure (through mechanical loading). The second "technology demonstration stage", now well underway, requires the manufacture and testing of full scale PFU prototypes, including the specified MB front surface toroidal bevelling (Section 3.2.1) and attachment to the steel support structure.

The thermal loading protocol in Stage 1 required that the W MB small-scale mock-ups demonstrate adequate thermal fatigue performance (in electron beam facilities) at both 10 MW m^{-2} and during a limited number of cycles up to twice this stationary heat flux (thus 20 MW m^{-2}), as a proxy for transient "divertor reattachment" events which might take place during the high power phases of ITER operation. It is during these latter tests (and never at 10 MW m^{-2}) that the "macro-cracking" (also denoted "self-castellation") phenomenon was observed on some MBs [120,121], in which a crack develops, usually near the centre of the MB (see inset in Fig. 17), where the thermal stress is highest due to the MB geometry (round cooling channel in a square MB). These cracks initiate at the heated surface, and can extend

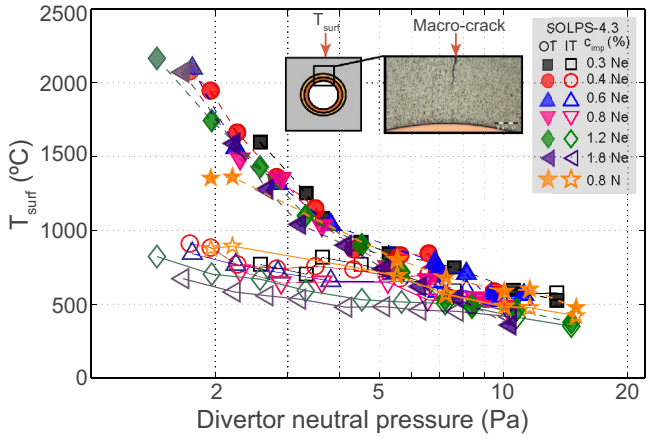

Fig. 17. Dependence on p_n of the surface temperature at the centre of an ITER W MB (6 mm thickness above the cooling channel) corresponding to the SOLPS-4.3 database values of $q_{\perp,pk}^{shp}$ at the IT and OT in Fig. 13 (thus with target tilting and MB shaping accounted for).

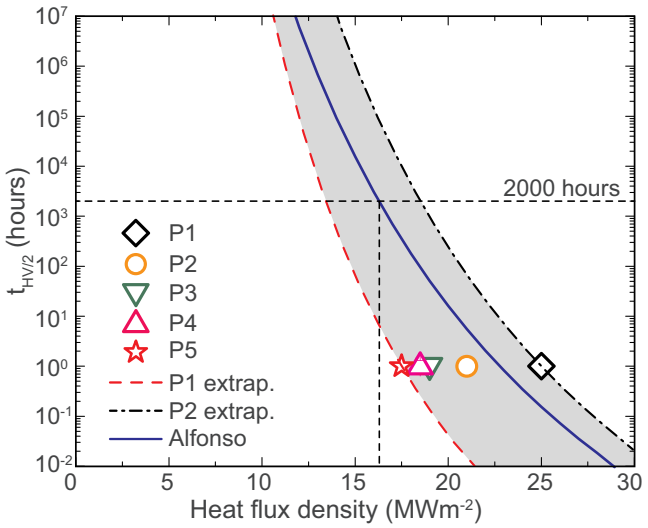

Fig. 18. Recrystallization time to a depth of 2 mm (using the time for material hardness to decrease by 50% as a proxy) as a function of the surface heat flux density at the centre of a 6 mm thick W MB. Points labelled P1-P5 are extracted from [127] for 5 samples of ITER grade W material annealed for 1 h at varying temperature. The shaded zone gives an indication of the uncertainty associated with the proposed method for estimation of the allowed exposure duration at given heat flux density (see main text). The horizontal dashed line corresponds to the approximate expected plasma exposure at burning plasma heat flux density through the FPO campaigns.

(depending on the number of loading cycles to 20 MW m^{-2}) to the pure copper interlayer between the W and the CuCrZr copper alloy cooling pipe [120]. This self-castellation does not seem to impair the thermal performance of the MB, but it does lead to the appearance of an exposed edge at the crack location (heights of up to 0.8 mm have been observed [122]). The response of this edge to high fluence plasma exposure and repeated transients is completely unknown at present.

The macro-cracking occurs as a result of recrystallization of the W near the MB surface due the high temperatures reached during the 20 MW m^{-2} loading. Recrystallization decreases the material hardness and strength, strongly affecting the thermal shock resistance and increasing brittleness, so that cracking can be promoted during heating or cooling of the MB for a given thermal cycle. The fact that the self-castellation is observed to occur only after a certain number of load cycles, suggests that a certain depth of material must have recrystallized before cracks appear and propagate [123]. Similar conclusions can be drawn from recent coupled thermal and fracture-mechanical 3-D finite element simulations [124], which found that for the ITER MB geometry and under conditions matching the engineering qualification tests, cracking occurs once a depth of about 2 mm into the material has undergone recrystallization.

These observations can be used to establish an approximate "operational budget" for the ITER divertor [125] based on material limits and their modification during plasma exposure, in particular due to recrystallization and specifically with the avoidance of self-castellation in mind. This is achieved by using the fact that recrystallization is a function of both temperature and time so that if the integral duration of exposure over lifetime is known, the allowed surface temperature before a given fraction of the material is recrystallized can be transformed into a maximum permissible stationary heat flux density over the exposure period. Fixing a budget in terms of bulk recrystallization may also have the possible added benefit of raising the threshold for surface cracking due to the fast, repetitive transient heat loads brought to the surface by ELMs (see Section 5) since the cracking itself is facilitated by the reduced mechanical strength of recrystallized material.

Fig. 17 makes the transformation of $q_{\perp,pk}^{shp}$ vs. p_n from the SOLPS-4.3 database to T_{surf} vs. p_n, using the data from Fig. 13, thus taking into account the impact of MB surface shaping and target tilting. Here T_{surf} is the surface temperature at the centre of the MB, where the macro-cracks usually form, and is thus the appropriate location at which to apply the recrystallization criterion. The transformation from $q_{\perp,pk}^{shp}$ to T_{surf} is performed using a simple linear relationship (T_{surf} (°C) = 85.6$q_{\perp,pk}^{shp}$ (MW m^{-2}) + 57) derived from finite element thermal simulations of the ITER reference MB design [36,123], with toroidal bevel, 6 mm W thickness at the block centre and using the nominal cooling parameters for MBs in the HHF regions of the vertical targets.

In [125], a methodology is proposed in which recrystallization kinetics is used to describe the temporal evolution of the recrystallization fraction, X, which in turn is related to the evolution of the material hardness, HV. It is assumed that the decrease in hardness due to recrystallization must be limited to half the total hardness drop occurring during full recrystallization, i.e. $\Delta HV/2$ is obtained when X = 0.5 (offset linear dependence of HV on X [125]), with an associated time, $t_{\Delta HV/2}$ at which this occurs for a given temperature (or surface heat flux density). Since the recrystallization kinetics of the W material to be used in ITER is not well characterized, published data from Alfonso [126] is used to estimate the dependence of $t_{\Delta HV/2}$ on temperature. This is shown as the full line in Fig. 18 for a depth of 2 mm into the material, as a function of surface heat flux density. To supplement this curve, additional data can be extracted from a materials characterization effort performed by the IO [127] which accompanied the full-W divertor qualification programme mentioned above [118]. Samples of five W products used in the manufacturing of the MB components tested within the this programme were annealed for 1 h at temperatures of 1300, 1500 and 1800°C then subject to tensile testing and hardness measurements. The times to reach X = 0.5 have been derived from these measurements for the five samples and are shown in Fig. 18, giving thus a single point in $t_{\Delta HV/2}$ (at 1 h). For the most and least sensitive to recrystallization, the full $t_{\Delta HV/2}$ curves have also been reconstructed assuming the same temperature dependence of the recrystallization kinetics as that from Alfonso et al. [126]. This provides a rough idea of the spread obtained from materials compliant with ITER specifications for tungsten.

It is now a simple matter to take the estimated ~2000 h of first divertor lifetime high performance exposure duration discussed in Section 2 (number rounded down from 2200 h for convenience) and associate this with a MB surface heat load. The dashed vertical line in Fig. 18, coupled with the approximate range provided by extrapolation of the isolated data points at $t_{\Delta HV/2}$ = 1 h thus indicates a heat flux density of ~16 ± 2.5 MW m^{-2} for the final MB design, in order not to

exceed the 50% hardness reduction and hence reduce the probability of macro-crack formation. This is considerably higher than the usual 10 MW m^{-2} often associated with the limit for stationary power density cycling of the ITER divertor MBs. It also brings some welcome margin in the event (Section 3.2) that future operators are obliged to accept higher heat fluxes.

Further detailed studies are underway at the time of writing to determine the recrystallization kinetics of the actual materials to be used for the inner and outer vertical targets. This will allow the estimates presented in Fig. 18 to be refined. It is of course important to bear in mind that this operational budget based on recrystallization does not account for the variety of additional factors which might influence W performance in ITER (e.g. He-induced brittleness and morphology changes, transient-induced melting, etc., see [125] for a comprehensive and recent review). Nevertheless, recrystallization is likely to be the most influential factor assuming transients can be adequately controlled, so that imposition of MB surface temperature limits should certainly be a key operational factor.

A final word is appropriate here on the subject of "transient reattachment", mentioned briefly in Section 3.2.1 in the context of MB surface shaping. From the point of view of engineering qualification of divertor MBs (e-beam heat flux tests), this is the phenomenon referred to as a "slow transient" (see e.g. [118,119,123]), in which the heat flux density is imagined to rise by a factor of 2 above the baseline stationary reference load of 10 MW m^{-2} and may remain at that level in quasi steady state, but for a limited number of cycles within the divertor lifetime [2]. These qualification tests typically subject the MBs to several hundred such cycles in comparison with the several thousand cycles for the baseline load. Physically, this is equivalent to moving to lower divertor neutral pressure in the p_n vs. $q_{\perp,pk}$ operating domain in Figs. 5a, 13 and 14. Such events may occur on relatively short timescales (hundreds of ms to seconds), but are not to be confused with the fast (ms) transients, ELMs and disruptions, discussed in the following section.

As discussed in Section 3.2.1, lower p_n corresponds to deposited power on the MB surface dominated by the thermal plasma and ion recombination components of the total heat load (Fig. 12), both sensitive to divertor target tilting and MB top surface shaping. At the lowest p_n (~2 Pa) in the SOLPS-4.3 database (with λ_q ~3.5 mm), $q_{\perp,pk}^{shp}$ ~ 25 MW m^{-2}, essentially independent of c_{Ne} for the same target tilt angle and MB toroidal bevel foreseen for ITER (Fig. 13). Should λ_q ~ 1 mm really occur at high I_p on ITER (Section 3.1.1), $q_{\perp,pk}^{shp}$ ~ 40 MW m^{-2} at p_n ~2 Pa (Fig. 14). These values should be compared with those obtained in very recent CHF thermal loading tests performed on a series of small-scale (3 mm W thickness) MB mock-ups provided by the European supplier of the ITER divertor IT [42]. In these experiments, the occurrence of CHF is detected by water leak on the mock-ups. Scaled to the ITER divertor MB final design thickness of 6 mm above the cooling channel, the results show that if the CHF margin of 1.4 which must be satisfied for the divertor MBs is to be preserved, the top surface heat flux density should not exceed ~20 MW m^{-2}. The corresponding CHF value of ~28 MW m^{-2} is also approximately the point at which bulk top surface melting would occur. Whilst CHF must of course be avoided at all costs, the same applies to bulk melting which, even for comparatively short timescales, will have very serious consequences (see [128] for an example of real tokamak tests). Note that according to Fig. 18, for operation at 20 MW m^{-2}, $t_{\Delta HV/2}$ ~ 1 h for the 2 mm recrystallization depth to be achieved.

5. Fast transients

Fast transient divertor loading is not generally an issue which strongly influences component design at the reactor scale, though the design should to some extent aim to mitigate the consequences where possible. The stored energy (W_{plasma} ~350 MJ) in ITER Q_{DT} = 10 baseline discharges is such that transient heat fluxes expected at the divertor targets due to large Type I ELMs and the disruption thermal quench will drive W far above melting temperatures and cannot be permitted to occur frequently.

A discussion of the risks from ELM and disruption-induced transients occupied the majority of the earlier ITER divertor physics basis paper, published soon after the 2013 decision to begin operations with a full-W divertor [2]. Much of what was stated there remains true and the final divertor design, 5 years on from that review retains, for example, the strong outer target baffle region toroidal chamfering intended to reduce the impact of downward vertical displacement events. In addition, the MB surface shaping, then only a proposal, has now been extensively studied and fixed into the design (see Section 3.2.1).

On the physics side, there have nevertheless been significant developments since 2013, particularly with regard both to an improved understanding of the expected Type I ELM target energy fluxes and to their impact on the W material. For the former, an important advance has been the publication of a new multi-machine (ASDEX Upgrade, JET and MAST) scaling [10] for the peak parallel outer target Type I ELM energy fluence, $\varepsilon_{||}$ obtained by coherent averaging over many similar ELMs of high resolution infra-red (IR) thermography: $\varepsilon_{||,scaling} = 0.28\frac{MJ}{m^2} n_{e,ped}^{0.75} T_{e,ped}^{1} \Delta W_{ELM}^{0.52} R^{1}$ with $n_{e,ped}$ [$x10^{20}$ m^{-3}], $T_{e,ped}$ [keV] the electron density and temperature at the H-mode pedestal top, ΔW_{ELM} the ELM energy loss (in %) relative to the plasma stored energy ($\Delta W_{ELM} = W_{ELM}/W_{plasma}$) and R the major radius [m]. The scatter of this data about the regression is roughly a factor of 3, for a range in $\varepsilon_{||}$ of more than two orders of magnitude in the database.

The proximity to unity of the exponents on $n_{e,ped}$ and $T_{e,ped}$, implies a linear dependence on pedestal top pressure, a feature which is reproduced by the simple model put forward in [10], which pictures the ELM pulse as the loss of energy stored in a toroidally uniform volume spanning a small region around the pedestal top which is connected by field line ergodization during the ELM to the divertor targets. This energy is assumed to empty onto the targets along the ergodized field lines on a free-streaming timescale. The model yields a compact expression for the ELM energy fluence, $\varepsilon_{||,model} \cong 6\pi p_{e,ped} R q_{edge}$, resembling the experimental scaling and in fact giving a good description of the lower bound of the regression (for smallest ΔW_{ELM}), with the upper bound (highest ΔW_{ELM}) being consistent with ~$3\varepsilon_{||,model}$. The good match of model and experiment allows the more ad hoc approach to the prediction of ELM target energy loads used in the original ITER Heat Load Specification [50,129], and subsequently adopted for the establishment of ELM control requirements on ITER [100], to be replaced by estimates obtained on a sounder physics basis.

Since the scaling was published, it has been found to apply also on the COMPASS tokamak (R = 0.56 m) using novel divertor target probe measurements [130] and from IR thermography on DIII-D [131], where the latter data support the suggestion that the rather large scatter in $\varepsilon_{||}$ found in the ASDEX Upgrade/JET/MAST may originate as a result of operation closer to the H-mode power transition threshold (as will be the case in ITER). This DIII-D work also reports an interesting inverse correlation of the ELM energy density with the toroidal mode number with the highest growth rate computed from linear stability analysis.

The data is yet relatively sparse, but observations on ASDEX Upgrade [10], DIII-D [131] and JET [132] generally support the scaling applicability also at the inner divertor target. On ASDEX Upgrade, an in-out symmetry of ~1.25 is observed in the peak target ELM energy fluences, consistent with approximate symmetry in the incoming $\varepsilon_{||}$ (since the projected area of the inner and outer target flux tubes differs by the inverse ratio of the toroidal fields at the inboard and outboard targets). The total ELM energy deposited on the IT in ASDEX Upgrade is about a factor of 2 higher than at the outboard since the ELM footprint mapped to the omp is twice as high as that for the OT (hence a broader inner target deposition profile) [132].

On ASDEX Upgrade, the scaling is equally found to apply to ELMs mitigated by magnetic perturbations, though the database is again still

relatively limited [10]. This latter point is of particular significance in the sense that because the pedestal pressure is the principal controlling parameter determining the peak target energy fluence in the empirical scaling, ELM mitigation (as opposed to suppression) by MP application will not itself reduce $\varepsilon_{||}$ for given ΔW_{ELM} if the pedestal pressure is preserved. In addition, an increased ELM frequency does not necessarily reduce the ELM-induced peak target load [133].

Applied to ITER, taking into account the total field line angles including divertor target and MB shaping ($\alpha = 4.2^{\circ}$, Fig. 3) the scaling [10] implies ELM energy densities on the OT of $\varepsilon_{\perp} \cong 0.36 \pm 0.18$ MJ m^{-2} for H-mode operation at 7.5 MA and 2.65 T ($T_{e,ped} = 2.35$ keV, $n_{e,ped} = 4 \times 10^{19}$ m^{-3} [5]), where the uncertainty simply accommodates the factor 3 variation in the experimental data about the regression. For burning plasmas at 15 MA and 5.3 T ($T_{e,ped} = 4.7$ keV, $n_{e,ped} = 8 \times 10^{19}$ m^{-3}), the same exercise yields $\varepsilon_{\perp} \cong 1.2 \pm 0.6$ MJ m^{-2}. For the inner target, the values will be higher owing to the higher field line incidence angle ($\alpha = 4.7^{\circ}$, Fig. 3) and the stronger toroidal field, but ranges are not given here since the scaling has not yet been fully established for the IT.

So what do these improved target energy density estimates imply for the W material of the ITER tungsten targets? In the original guidelines established by the IO to ensure adequate PFC lifetime [100], a maximum ELM-induced target energy flux density of 0.5 MJ m^{-2} on the front surface of the MBs was fixed on the basis of extrapolations from experiments in plasma gun (QSPA) facilities. At these energy densities, edge melting of W macrobrush targets (as a proxy for the discrete MB structure) was avoided, with an approximate margin of a factor 2 before full surface melting.

The rather extensive ion orbit modelling referred to in Section 3.2.1 [37] used to assess the requirement for MB shaping can be combined with the new scaling on $\varepsilon_{||}$ to provide revised estimates of tolerable transient energy fluence before the onset of melt damage. This has been performed in [37], Fig. 49 of which has been adapted and is reproduced here in Fig. 19, in particular modifying the ordinate to account for the monoblock top surface shaping and global target tilting. It shows the ELM energy fluence which raises some point on the top surface and the upper TG edges of ITER outer target W MBs to melting temperature as a function of I_p for three pairs of I_p and B_{φ} at $q_{95} = 3$ ((5 MA, 1.76 T), (7.5 MA, 2.65 T) and (15 MA, 5.3 T)). The first two are the key points identified in the IRP [6] as operating points for H-mode explorations in the PFPO phases (see Section 2).

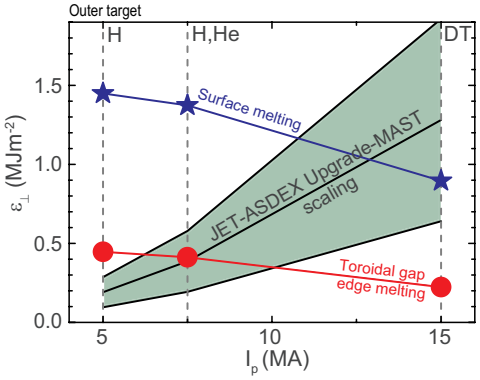

Fig. 19. Outer target ELM energy fluences which lead to MB top surface and toroidal gap edge melting at 3 representative operating points within the IRP, corresponding to non-active H-modes at 5 MA/1.8 T in H, 7.5 MA/2.65 T in He or D and 15 MA/5.3 T in DT. The values are computed from ion orbit modelling, including a full thermal model of the MB subject to appropriate inter-ELM heat loads at these operating points. Monoblock surface shaping and target tilting are included, unlike in Fig. 49 of [37], from which the figure is adapted. The expected $\varepsilon_{\perp}$ from a new empirical scaling [10] is also included for $\Delta W_{ELM} = 5.4\%$ (as in [10]), with associated factor 3 spread of the experimental data about the regression (shaded area).

The new $\varepsilon_{||}$ scaling, projected onto the target, is also included for a single value of $\Delta W_{ELM} = 5.4\%$ (matching the example value chosen in Figs. 2 and 3 in [10] for extrapolation to ITER) along with the range (shaded region) corresponding to the factor 3 spread of the scaling data about the regression. An important feature of the computed melt onset energy densities is that they account not only for ion orbit effects to obtain the TG loads, but also include a thermal model of the shaped MB to calculate the steady state MB surface temperature distribution resulting from a specified inter-ELM surface power flux density appropriate to each value of I_p (see Table 4 in [37]). The computed ELM-induced temperature excursion thus starts from a realistic baseline. Any point falling within or below the shaded region implies that melting will occur if the new empirical ELM energy fluence scaling applies on ITER. Thus, for uncontrolled ELMs at $\Delta W_{ELM} = 5.4\%$ (corresponding to $W_{ELM} \sim 19$ MJ on ITER at $Q_{DT} = 10$), both TG and top surface melting are unavoidable, whilst for non-active phase H-modes at $I_p \leq 7.5$ MA, surface melting should not occur and TG edge melting is either marginal (7.5 MA) or avoided (5 MA).

Compared to the previous specifications for ITER, the new scaling does not in any way alleviate the requirement for strong ELM control/suppression at high performance in ITER from the point of view of PFC lifetime. Bearing in mind the proposed operating restrictions discussed in Section 4 in the context of recrystallization, it is clear that repeated shallow surface melting is to be avoided as much as possible. In fact, resolidified W surfaces show very similar damage behaviour to recrystallized material [134]. It should also be noted that the curves in Fig. 19 give only an example for a single ELM size and only for the outer target (the energy densities will be higher at the inner target – see above). Moreover, the analysis is focused only on melt limits and takes no account of the issue of W sputtering and transport due to the ELM. An uncontrolled ELM at $\Delta W_{ELM} = 5.4\%$ is a very large energy loss, even at lower performance, and such events will occur at low frequency. They are also likely to induce a strong vapour shield in front of the target which should mitigate some of the incoming heat flux. However, as shown in the parametric study of [5], which also adopts the new empirical ELM energy fluence scaling, ELM-induced W sputtering is expected to set lower limits on allowed natural ELM sizes (and thus on the required ELM control) than those due to melting.

Fig. 19 provides an extremely low threshold for TG edge melting ($\varepsilon_{\perp} \sim 0.2$ MJ m^{-2}) for 15 MA H-mode operation. This is about a factor 2 higher than the fatigue damage threshold, ~ 0.1 MJ m^{-2} (formation of thermal shock crack networks) for W surfaces with longitudinal grain orientation (as in ITER) found in electron beam tests after 10^6 ELM-like pulses on a surface with 700°C base temperature [135]. When similar experiments are performed on recrystallized material, this threshold can fall still further [136]. Note that for the kinds of ELM frequencies (tens of Hz) required for controlled ELMs which meet the various criteria set by surface melting and W production [5], 10^6 transients will be achieved in $\lesssim$100 reference burning plasmas at $Q_{DT} = 10$. According to the empirical scaling, values of ΔW_{ELM} which produce such low target energy densities under burning conditions are at the level of 0.15%. Such Type I ELM sizes are not seen naturally in present experiments, implying that complete suppression, the goal of ELM control on ITER, is indeed required.

Regarding the surface cracking, it is known that this can induce crack propagation into the material [136], possibly linked to recrystallization driven by the transient heating. How this is further influenced by operation under relevant plasma loading conditions (e.g. high particle fluences, mixtures with He etc.) is currently unknown [125]. Concerning ELM-induced TG edge melting, although this has not yet been directly observed experimentally, it has been seen under stationary conditions in recent dedicated experiments on the COMPASS tokamak [137].

Understanding of W melt dynamics under tokamak fast transients, particularly ELMs, has advanced considerably in the past 5 years, with dedicated experiments first on JET [138] then later on ASDEX Upgrade

[139]. The MEMOS 3D melt code has been used to model the experimental findings in both cases, but has undergone radical improvement in particular during the course of the past two years guided by experimental benchmarking activities on ASDEX Upgrade [140,141]. Unfortunately, the shallow water approximation, which is the fundamental assumption in MEMOS 3D, makes it difficult to apply it to the case of TG edge melting and a new simulation tool is required. Moreover, such theoretical estimates need experimental support, particularly regarding the long term effect of plasma exposure on damaged edges.

On the subject of disruptions, there has been very little advance in recent years concerning divertor interactions. The scenarios identified in [2] remain valid. In the early years of ITER operation, it is the Be first wall which is at highest risk, as a result both of the heavy potential loads during the current quench phase, even at comparatively low I_p, and the lower melting temperature of Be in comparison with W [142]. Runaway electrons pose a serious threat, not just from the point of view of PFC damage, but also to the PFC cooling channels. The development of a comprehensive disruption mitigation system (DMS) based on shattered pellet injection to reduce PFC thermal loads and prevent the formation of runaway electrons, is a major priority at the IO [143].

By the time in the Research Plan that plasma stored energies become significant enough for disruption thermal quench loads to cause appreciable melt damage in the HHF regions of the divertor targets, considerable experience of disruption avoidance and mitigation should have been accumulated. This does not of course eliminate the possibility of such damage, but some recent new simulations with the TOKES code have highlighted the potentially very strong benefits of W vapour shielding at the targets in reducing both the melt pool depth and extent for deposited energy densities above a given threshold [144]. These simulations have been to some extent validated against some rather old measurements of W shield plasma dynamics on the 2MK-200 plasma gun facility [145]. New, improved experiments, including the study of the energy threshold, spatial extent, temperature and density, velocity and duration of the shield plasma, together with a temporal and spectral measurements of the W plasma radiation are the target of an ongoing contract with the IO on an upgrade (MK-200UG) of the 2MK-200 device.

6. Conclusions and key areas for further R&D

The ITER tungsten divertor, the largest and most ambitious of its kind ever to be constructed, is on the eve of procurement, with the design essentially complete. To mark the occasion, this paper has tried to describe some of the main aspects of the physics basis which have determined the design and to highlight a number of the key issues which still remain for future studies, both theoretical and experimental, in the coming years before ITER operation begins. It also makes use of the release, in late 2018 [6], to the ITER Community of a very significant update of the ITER Research Plan, revised on the basis of the new staged approach to ITER operations, to provide more quantitative estimates of the expected plasma exposure which the first divertor will be required to survive over its lifetime. In the IRP, the latter is now estimated to be around 6 years of fusion power operation beyond the initial non-active phase campaigns. This corresponds to ~2000 h of projected high performance plasmas, during which the divertor will need to function in its intended, partially detached operating mode, with extrinsic impurity seeding used as the principal mechanism for volumetric power dissipation to maintain acceptable target stationary heat flux densities.

Making use of the database of SOLPS-4.3 simulations compiled for “carbon-free” Ne and N-seeded operation under nominal burning plasma conditions (P_{SOL} = 100 MW) [3], the paper has focused on the accessible domain in terms of two key operational parameters, divertor neutral pressure and peak target heat flux density, each tightly linked to the other. Some first-of-a-kind simulations for the metal environment with the ITER-hosted, and significantly enhanced SOLPS version SOLPS-ITER, are also included, giving a first glimpse of the impact of fluid drifts on the target heat fluxes.

Particular attention is paid to a discussion of the partially detached state, leaving aside the (important) issue of compatibility of the divertor operating condition with core plasma performance. The latter has been the subject of a great deal of well documented study in the years leading up to finalization of the divertor design. The detachment behaviour features all the classic ingredients of what is expected for a vertical target configuration (and this is indeed the main reason for this choice of divertor geometry).

At high power, detachment is not possible without the use of extrinsic species used for volumetric power dissipation. Given the potential restrictions on duty cycle linked with the exhaust of tritiated ammonia (Section 3.1.4), avoidance of nitrogen on ITER would be preferable. Under partially detached conditions, nitrogen is seen to be favourable experimentally on present devices from the point of view of plasma performance, whilst the SOLPS-4.3 simulations discussed here indicate that both Ne and N will be effective on ITER. A companion study [78] using SOLPS-ITER has for the first time been able to examine the effect of drifts of ITER under high performance conditions (thus at B_φ = 5.3 T) with Ne and N seeding. This cannot be performed with the SOLPS-4.3 physics model and has required very considerable technical effort to make possible with SOLPS-ITER in terms of code speed-up. Very similar plasma boundary solutions to those obtained with SOLPS-4.3 are found for high sub-divertor neutral pressures, indicating a rather weak impact of drifts under these conditions.

At lower pressures, however, the drift solutions find much larger out-in asymmetries, making such operation undesirable since outer target heat flux densities can rapidly approach difficult levels. This is exacerbated by the relatively long timescales for response of the gas injection systems on ITER, where distances from gas valve boxes and entry points into the vacuum vessel are necessarily very large. Very rapid reaction times (e.g. in terms of adding more impurity) are thus not possible. Moreover, as shown in [146], for Ne impurity, residence times decrease rapidly with increasing divertor neutral pressure due to the increased pumping efficiency at low divertor plasma temperature. A very important effort will need to be dedicated during ITER operation to put in place and test robust detachment feedback control schemes. This is fully accounted for in the revised ITER Research Plan [6]. In the event that such control is lost and divertor heat loads increase beyond what can be recovered by the actuators in place, disruption mitigation will be the last line of defence.

Importantly, the drift runs also indicate a size effect linked to the position of the fuel flow reversal (stagnation) point with respect to the target location and the higher separatrix plasma temperatures accessible on ITER. This translates to a higher divertor T_e and means that the charge states of seeded impurity responsible for the bulk of the divertor radiation are located well within the divertor volume. There are also hints of a direct influence on impurity screening of the near separatrix heat flux channel width in the divertor.

A key message of this work has been to demonstrate that properly taking into account the now fixed values of divertor target tilting and monoblock top surface shaping, the possibility of much narrower than previously thought SOL heat flux channels and the impact, just mentioned, of drifts, pushes the allowed operating point to higher neutral pressure, and hence deeper detachment. At the same time, however, now that the monoblock design is complete, a new look at permissible stationary heat loads from the perspective of the W material recrystallization and the requirement to avoid monoblock self-castellation, yields values ~50% higher than the historically adopted ~10 MW m^{-2} maximum stationary load. Overall, higher p_n is likely to be the preferred target for future burning plasma operation to ensure that the W surface stays as far below recrystallization temperature as possible. This is the region where in-out stationary heat flux density asymmetries are predicted to be lowest (so that one target does not dominate the overall divertor performance) and where the effects of

component shaping are least felt on the target heat fluxes. Higher pressures would seem to be mandatory if really the heat flux channel width will be as small on ITER at high plasma current as the current empirical scaling suggests.

Moving in the other direction, to lower divertor pressure, is where the combined effects of target tilting and monoblock shaping, drifts and lower than previously expected heat flux channel widths will be most strongly felt. Out-in target asymmetries are predicted to increase strongly and it is at lower pressure that the target heat flux is dominated by thermal plasma and plate ion recombination contributions, both increasing with increasing magnetic field incidence angles. Tighter control is thus required to avoid any kind of slow transient excursion pushing to lower pressure since surface power flux densities can easily approach those corresponding to the maximum values allowed ($\sim$20 MW m^{-2}) if the factor 1.4 margin to critical heat flux at the monoblock cooling channels which ITER requires is to be maintained. Critical heat flux itself is reached at $\sim$28 MW m^{-2} for the final ITER monoblock design, corresponding approximately to the onset of bulk top surface melting. Both are to be avoided at all costs.

Pushing to deeper detachment means operating closer to the point at which the ionization front may move (perhaps rapidly) towards the X-point, leading to fluctuations in target power fluxes which will be difficult to control on a device of ITER's size. This may also lead to a possible deleterious impact on core confinement, especially given the proximity to the H-mode power transition threshold at which ITER will operate, even for burning plasmas.

Regarding fast transient heat loads, there is little one can do to design for the very heavy energy fluences which unmitigated disruptions at high stored energy on ITER can potentially deposit on the divertor targets. In recent years, driven in part by the need to decide on the issue of monoblock surface shaping, the fidelity with which W melt motion in the tokamak environment can be modelled has considerably improved, so that a better idea of the likely surface damage due to transient melting (due both to disruptions and ELMs) can at least be provided. Moreover, beyond a certain, rather low threshold in stored plasma energy, vapour shielding is now thought to offer a potentially strong mitigation of the incoming heat flux to a W surface [144]. Melting would still occur, but to a much smaller degree. It is clear, however, that repetitive heavy transients, quite apart from the surface melting they may cause, would rapidly eliminate any benefit gained from careful attempts to avoid recrystallization of the W near surface during normal plasma operation.

For Type I ELMs, which are seen ubiquitously on current devices during the baseline H-mode operation which ITER targets for $Q_{DT} = 10$ performance, mitigation by several factors is still required if monoblock surface melting is to be avoided, even taking into account the new empirical scaling, more favourable for ELM target energy fluence on ITER than previous estimates used to specify ELM control requirements. If ELM-induced melting of toroidal gap edges, which cannot be fully protected at both ITER targets by monoblock shaping, is to be avoided, the tolerable plasma energy loss per ELM falls by a further factor $\sim$3. Coincidentally, the energy fluences which are calculated to drive toroidal gap edge melting are very close to those observed in laboratory (e-beam) tests to provoke micro-cracking of W surfaces at high transient pulse numbers approaching, but still at least an order of magnitude short, of those expected on ITER for mitigated ELMs during the first divertor lifetime.

A clear way to avoid these uncertain material issues is complete transient suppression. This is not realistically achievable, since it is impossible to avoid all ELM or disruptive transients during the process of learning how to operate a new device, particularly one on the ITER scale. However, ELM suppression is the goal of the ELM control coil set with which ITER is being equipped. The magnetic perturbations produced by these coils break the toroidal symmetry of the target loading which is the fundamental assumption of all the 2-D plasma boundary simulations constituting the vast majority of ITER divertor simulations to-date. With the advent of enhancements to the 3-D EMC3-Eirene plasma boundary code, it is now becoming possible to explore stationary divertor power loading in the presence of these 3-D fields with realistic plasma response. Early results, referred to in this paper and deploying the first of these improvements, demonstrate that matters can become considerably more difficult when heat fluxes reaching the targets at locations distant from the unperturbed strike point region do so from regions within the core plasma.

Compared with the last physics basis, published in 2013 following the decision to switch to a full W variant for the first ITER divertor [2], there has been a very substantial increase in R&D throughout the community in both physics and materials which have helped to consolidate the design and significantly improve scope and understanding. This paper has tried to reflect some of this advance whilst at the same time indicating where more research is required. To conclude the article, some of these key areas are listed below in abbreviated form, beginning with plasma physics issues and ending with a point on outstanding (W) material aspects, also raised explicitly in the review of [125]:

- Improve understanding of the expected near-SOL heat flux width at high plasma current in ITER;
- Extend database of ITER divertor simulations with fluid drifts, including cases with reduced transport to examine consequences of very narrow λ_q;
- Continue numerical and experimental studies to confirm that N and Ne will be equally effective divertor radiators for ITER at high performance, but only within $\sim$factor 2 of the H–L transition threshold power. In parallel, improve understanding (experiment and simulation) of ammonia formation and transport in high performance divertors with metal PFCs;
- Explore the consequences of operation at very high pressure (deep detachment degree) with low Z seeding in ITER $\rightarrow$ stability and dynamics of radiation fronts in the divertor and development of methods for detachment control using the same sensors and actuators as will be available on ITER.
- Pursue basic understanding of divertor detachment physics, in particular the link between target quantities and distributed pressure/power losses, the precise role/importance of volume recombination in reducing target ion flux and the behaviour of upstream density with impurity concentration. A key long term goal, for ITER and reactor design, is the development of reduced models which can capture the complexity of divertor function under ITER-like conditions, but still be amenable for use in global transport analyses (integrated modelling) which require much more rapid boundary solvers than can be provided by SOLPS-type codes;
- Significantly expand efforts to simulate the ITER divertor target power loads in the presence of 3-D fields for ELM control under high performance conditions with extrinsic seeding and realistic plasma response;
- Extend the ELM parallel energy density scaling to include more cases of mitigated ELMs and data at both inner and outer divertor targets and improve understanding of the origins of the scatter in the data for the peak target energy density. Confirm experimentally the phenomenon of ELM-induced toroidal gap loading and investigate the dissipation of ELM energy due to dissipative divertor plasma buffering;
- Quantify the contribution of W plasma vapour shielding to the reduction of incoming heat loads under heavy transients (experiment-theory benchmarking);
- Understand the effect of plasma and neutron irradiation on W thermo-mechanical properties and quantify the link between plasma-wall interaction induced material damage and material lifetime, ultimately leading to the development of a multi-scale model for PFC lifetime prediction (including plasma and neutron effects).

Declaration of interests

The authors declare that they have no known competing financial interests or personal relationships that could have appeared to influence the work reported in this paper.

Acknowledgements

The views and opinions expressed herein do not necessarily reflect those of the ITER Organization. ITER is the nuclear facility INB 174. Portions of this work were performed under the auspices of the U.S. Department of Energy under grants DE-SC0012315 and DE-SC0013911, and by funding of the Department of Engineering Physics and of the College of Engineering at the University of Wisconsin-Madison, USA. The work of the SPbPU group was supported by the Russian Science Foundation, grant no. 17-12-01020. Several of the co-authors have contributed within the framework of the ITER Scientist Fellowship Network (ISFN). The authors would like to specifically acknowledge the very significant contribution to the ITER divertor design activity made over more than 2 decades by H. D. Pacher and G. W. Pacher.

References

[1] R.A. Pitts, et al., Phys. Scr. T138 (2009) 014001.
[2] R.A. Pitts, et al., J. Nucl. Mater 438 (2013) S48.
[3] H.D. Pacher, et al., J. Nucl. Mater 463 (2015) 591.
[4] R. Dux, et al., Nucl. Mater. Energy 12 (2017) 28.
[5] A.R. Polevoi, et al., Nucl. Fusion 58 (2018) 056020.
[6] "ITER Research Plan within the Staged Approach", ITER Technical Report ITR-18-003 available at: https://www.iter.org/technical-reports.
[7] H.D. Pacher, et al., J. Nucl. Mater 390–391 (2009) 259.
[8] G. Janeschitz, et al., Nucl. Fusion 42 (2002) 14.
[9] M. Merola, et al., Fusion Eng. Des 75–79 (2005) 325.
[10] T. Eich, et al., Nucl. Mater. Energy 12 (2017) 84.
[11] A.S. Kukushkin, et al., J. Nucl. Mater 290-293 (2001) 887.
[12] A.S. Kukushkin, et al., Nucl. Fusion 42 (2002) 187.
[13] A.S. Kukushkin, H.D. Pacher, Plasma Phys. Control. Fusion 44 (2002) 931.
[14] H.D. Pacher, et al., J. Nucl. Mater 313-316 (2003) 657.
[15] A.S. Kukushkin, et al., Nucl. Fusion 43 (2003) 716.
[16] A.S. Kukushkin, et al., Fusion Eng. Des. 65 (2003) 355.
[17] A.S. Kukushkin, et al., Nucl. Fusion 45 (2005) 608.
[18] A.S. Kukushkin, et al., J. Nucl. Mater 337-339 (2005) 17.
[19] A.S. Kukushkin, et al., Nucl. Fusion 47 (2007) 698.
[20] A.S. Kukushkin, et al., J. Nucl. Mater 363-365 (2007) 308.
[21] G.W. Pacher, et al., Nucl. Fusion 48 (2008) 105003.
[22] A.S. Kukushkin, et al., Nucl. Fusion 49 (2009) 075008.
[23] H.D. Pacher, et al., J. Nucl. Mater 415 (2011) S492.
[24] G.W. Pacher, et al., Nucl. Fusion 51 (2011) 083004.
[25] A.S. Kukushkin, et al., J. Nucl. Mater 415 (2011) S497.
[26] A.S. Kukushkin, et al., Fusion Eng. Des 86 (2011) 2865.
[27] A.S. Kukushkin, et al., Nucl. Fusion 53 (2013) 123024.
[28] A.S. Kukushkin, et al., J. Nucl. Mater 438 (2013) S203.
[29] A.S. Kukushkin, H.D. Pacher, Contrib. Plasma Phys 56 (2016) 711.
[30] G.W. Pacher, et al., Plasma Phys. Control. Fusion 46 (2004) A257.
[31] G.W. Pacher, et al., Nucl. Fusion 45 (2005) 581.
[32] H.D. Pacher, et al., J. Nucl. Mater 363-365 (2007) 400.
[33] A.S. Kukushkin, H.D. Pacher, Nucl. Fusion 56 (2016) 126012.
[34] S. Carli, et al., Nucl. Fusion 58 (2018) 126022.
[35] M. Merola, et al., Fusion Eng. Des 89 (2014) 890.
[36] R.A. Pitts, et al., Nucl. Mater. Energy 12 (2017) 60.
[37] J.P. Gunn, et al., Nucl. Fusion 57 (2017) 046025.
[38] T. Hirai, et al., Fusion Eng. Des 127 (2018) 66.
[39] K. Heinola, et al., Phys. Scr. T167 (2016) 014075.
[40] A. Widdowson, private communication.
[41] S. Brezinsek, et al., Nucl. Fusion 53 (2013) 083023.
[42] F. Escourbiac et al., "Assessment of Critical Heat Flux margin on the tungsten monoblock design of the ITER divertor vertical targets", Fus. Eng Des., in press: https://doi.org/10.1016/j.fusengdes.2019.03.094.
[43] F. Koechl, et al., Nucl. Fusion 57 (2017) 086023.
[44] S.I. Krasheninnikov, A.S. Kukushkin, J. Plasma Phys 83 (2017) 155830501.
[45] R. A. Pitts et al., "The ITER divertor concept: physics and engineering design", 1st IAEA Technical Meeting on Divertor Concepts, 29 Sept. – 2 Oct, Vienna, Austria, see: http://www-naweb.iaea.org/napc/physics/meetings/TM49934.html.
[46] F. Imbeaux, et al., Nucl. Fusion 55 (2015) 123006.
[47] S. Wiesen, et al., J. Nucl. Mater 463 (2015) 280.
[48] X. Bonnin, et al., Plasma Fusion Res. 11 (2016) 1403102.
[49] M. Shimada, et al., Nucl. Fusion 47 (2007) S1.
[50] R.A. Pitts, et al., J. Nucl. Mater 415 (2011) S957.
[51] G.T.A. Huijsmans, A. Loarte Nucl, Fusion 53 (2013) 123023.
[52] K. Schmid, et al., Nucl. Fusion 55 (2015) 053015.
[53] S. Maruyama et al., Proceedings of the 22nd IAEA Fusion Energy Conference, San Diego, USA 8–13 October 2012, paper ITR/P5-24.
[54] J.-S. Park et al., in preparation forNucl. Fusion.
[55] V. Kotov, et al., Plasma Phys. Control. Fusion 50 (2008) 105012.
[56] T. Eich, et al., Nucl. Fusion 53 (2013) 093031.
[57] R.J. Goldston, Nucl. Fusion 52 (2012) 013009.
[58] V. Rozhansky, et al., Plasma Phys. Control. Fusion 60 (2018) 035001.
[59] J. Adamek, et al., Nucl. Fusion 57 (2017) 022010.
[60] E Vekshina, et al., Plasma Phys. Control. Fusion 58 (2016) 085007.
[61] D. Brunner, et al., Nucl. Fusion 58 (2018) 094002.
[62] C.S. Chang, et al., Nucl. Fusion 57 (2017) 116023.
[63] C. S. Chang et al., 27th IAEA Fusion Energy Conference, 22–27 October 2018, Gandhinagar, India, paper: IAEA-CN-258-TH/P7-22.
[64] X. Q. Xu et al., 27th IAEA Fusion Energy Conference, 22–27 October 2018, Gandhinagar, India, paper: IAEA-CN-258-TH/P7-21, submitted to Nucl. Fusion.
[65] A.S. Kukushkin, et al., Contrib. Plasma Phys. 40 (2000) 233.
[66] A.A. Pshenov, et al., Phys. Plasmas 24 (2017) 072508.
[67] R.A. Pitts, et al., J. Nucl. Mater 337-339 (2005) 146.
[68] A. Kallenbach, et al., Nucl. Fusion 55 (2015) 053026.
[69] P.C. Stangeby, Plasma Phys. Control. Fusion 60 (2018) 044022.
[70] A. Loarte, et al., J. Nucl. Mater 463 (2015) 401.
[71] A. Drenik, et al., Nucl. Fusion 59 (2019) 046010.
[72] S. Touchard, et al., Nucl. Mater. Energy 18 (2019) 12.
[73] M. Bernert, et al., Nucl. Mater. Energy 12 (2017) 111.
[74] C. Giroud, et al., Plasma Phys. Control. Fusion 57 (2017) 035004.
[75] A. Loarte, et al., Phys. Plasmas 18 (2011) 056105.
[76] L.L. Lengyel, Analysis of Radiating Boundary Layers, (September 1981) IPP Report 1/191 Max-Plank Institut fuer Plasmaphysik.
[77] D. Moulton et al., to be submitted to Nucl. Fusion.
[78] E. Sytova, et al., Nucl. Mater. Energy 19 (2019) 72.
[79] I. Senichenkov, et al., Plasma Phys. Control. Fusion 61 (2019) 045013.
[80] B. Lipschultz, et al., Fusion Sci. Technol. 51 (2007) 369.
[81] P.C. Stangeby, C. Sang, Nucl. Fusion 57 (2017) 056007.
[82] V. Kotov, D. Reiter, Plasma Phys, Control. Fusion 51 (2009) 115002.
[83] J.-S. Park, et al., Nucl. Fusion 58 (2018) 126033.
[84] W. Eckstein, "Reflection (Backscattering)", IPP Report 17/12 Max-Planck Institut fuer Plasmaphysik, August 2009.
[85] M. Komm, et al., Nucl. Fusion 57 (2017) 126047.
[86] J. P. Gunn et al., accepted for publication in Nucl. Fusion.
[87] J.P. Gunn, et al., Nucl. Mater. Energy 12 (2017) 75.
[88] I.H. Hutchinson, et al., Plasma Phys. Control. Fusion 37 (1995) 1389.
[89] E. Kaveeva, et al., Nucl. Fusion 58 (2018) 126018.
[90] E. Kaveeva et al., in preparation for submission to Nucl. Fusion.
[91] A. Jarvinen, et al., Phys. Rev. Lett. 121 (2018) 075001.
[92] K. Ghoos, et al., Nucl. Fusion 59 (2019) 026001.
[93] T. Eich, et al., Nucl. Fusion 58 (2018) 034001.
[94] A. Kallenbach, et al., Nucl. Mater. Energy 18 (2019) 166.
[95] S. Henderson, M. Bernert, private communication.
[96] F. Reimold, et al., Nucl. Fusion 55 (2015) 034004.
[97] T.E. Evans, et al., Phys. Rev. Lett. 92 (2004) 235003.
[98] W. Suttrop, et al., Nucl. Fusion 58 (2018) 096031.
[99] Y. In, et al., Nucl. Fusion 57 (2017) 116054.
[100] A. Loarte, et al., Nucl. Fusion 54 (2014) 033007.
[101] M.E. Fenstermacher, et al., Phys. Plasmas 15 (2008) 056122.
[102] O. Schmitz, et al., Plasma Phys. Control. Fusion 50 (2008) 124029.
[103] C. Paz-Soldan, et al., Phys. Rev. Lett. 114 (2015) 105001.
[104] R. Nazikian, et al., Phys. Rev. Lett. 114 (2015) 105002.
[105] H. Frerichs, et al., Physics Plasmas 22 (2015) 072508.
[106] Y. Feng, et al., Contrib. Plasma Phys 54 (2014) 426.
[107] Y. Feng, et al., Plasma Phys. Control. Fusion 59 (2017) 034006.
[108] H. Frerichs, et al., Comput. Phys. Commun. 188 (2015) 82.
[109] O. Schmitz, et al., Nucl. Fusion 56 (2016) 066008.
[110] H. Frerichs, et al., Nucl. Mater. Energy 18 (2019) 62.
[111] F. Schluck et al., 27th IAEA Fusion Energy Conference, 22–27 October 2018, Gandhinagar, India, paper IAEA-CN-258-TH/P1-5, submitted to Nucl. Fusion.
[112] H. Frerichs et al., submitted toPhys. Rev. Lett.
[113] Y.Q. Liu, et al., Phys. Plasmas 7 (2000) 3681.
[114] L. Li, et al., Plasma Phys. Control. Fusion 59 (2017) 044005.
[115] J. Li, et al., Nat. Phys. 9 (2013) 817.
[116] J.W. Ahn, et al., Plasma Phys. Control. Fusion 59 (2017) 084002.
[117] M. Faitsch, et al., Plasma Phys. Control. Fusion 61 (2019) 014008.
[118] T. Hirai, et al., Phys. Scr. T159 (2014) 014006.
[119] T. Hirai, et al., J. Nucl. Mater 463 (2015) 1248.
[120] G. Pintsuk, et al., Fusion Eng. Des. 88 (2013) 1858.
[121] T. Hirai, et al., Nucl. Mater. Energy 9 (2016) 616.
[122] G. Pintsuk, et al., Fusion Eng. Des. 98-99 (2015) 1384.
[123] S. Panayotis, et al., Fusion Eng. Des. 125 (2017) 256.
[124] M. Li, J.H. You, Fusion Eng. Des. 101 (2015) 1.
[125] G. De Temmerman, et al., Plasma Phys. Control. Fusion 60 (2018) 044018.
[126] A. Alfonso, et al., J. Nucl. Mater 455 (2014) 591.
[127] S. Panayotis, et al., Nucl. Mater. Energy 12 (2017) 200.
[128] J.W. Coenen, et al., Nucl. Fusion 51 (2011) 083008.
[129] A. Loarte, et al., 22nd IAEA Fusion Energy Conference, Geneva, Switzerland, 13–18 October, Vienna: IAEA, 2008paper IT/P6-13.
[130] J. Adamek, et al., Nucl. Fusion 57 (2017) 116017.

[131] M. Knolker, et al., Nucl. Fusion 58 (2018) 096023.
[132] A. Scarabosio et al., "ELM energy loads in hydrogen and helium in JET", 24th Meeting of the ITPA Scrape-Off Layer and Divertor Topical Group, Univ. of York, UK30 May – 2 June , 2017.
[133] B. Sieglin, et al., Phys. Scr. T170 (2017) 014071.
[134] Th. Loewenhoff, et al., Nucl. Mater. Energy 9 (2016) 165.
[135] Th. Loewenhoff, et al., Fusion Eng. Des. 87 (2012) 1201.
[136] M. Wirtz, et al., Nucl. Mater. Energy 12 (2017) 148.
[137] R. Dejarnac, et al., Nucl. Fusion 58 (2018) 066003.
[138] J.W. Coenen, et al., Nucl. Fusion 55 (2015) 023010.
[139] K. Krieger, et al., Nucl. Fusion 58 (2018) 026024.
[140] E. Thoren, et al., Phys. Scr. T170 (2017) 014006.
[141] E. Thoren, et al., Nucl. Mater. Energy 17 (2018) 194.
[142] M. Lehnen, J. Nucl. Mater 463 (2015) 39.
[143] M. Lehnen et al., 27th IAEA Fusion Energy Conference, 22-–27 October 2018, Gandhinagar, India, paper: IAEA-CN-258-EX/P7-12.
[144] S. Pestchanyi, et al., Fusion Eng. Des. 109-111 (2016) 141.
[145] S. Pestchanyi, et al., Fusion Eng. Des. 124 (2017) 401.
[146] X. Bonnin, et al., Nucl. Mater. Energy 12 (2017) 1100.